The Astrophysical Journal, 668:331–347, 2007 October 10
© 2007. The American Astronomical Society. All rights reserved. Printed in U.S.A.

STRUCTURE OF W3(OH) FROM VERY HIGH SPECTRAL RESOLUTION OBSERVATIONS OF 5 CENTIMETER OH MASERS

Vincent L. Fish[1] and Loránt O. Sjouwerman
National Radio Astronomy Observatory, 1003 Lopezville Road, Socorro, NM 87801; vfish@nrao.edu
Received 2007 April 17; accepted 2007 June 22

ABSTRACT

Recent studies of methanol and ground-state OH masers at very high spectral resolution have shed new light on small-scale maser processes. The nearby source W3(OH), which contains numerous bright masers in several different transitions, provides an excellent laboratory for high spectral resolution techniques. We present a model of W3(OH) based on European VLBI Network (EVN) observations of the rotationally excited 6030 and 6035 MHz OH masers taken at 0.024 km s^{-1} spectral resolution. The 6.0 GHz masers are becoming brighter with time and show evidence for tangential proper motions. We confirm the existence of a region of magnetic field oriented toward the observer to the southeast and find another such region to the northeast in W3(OH), near the champagne flow. The 6.0 GHz masers trace the inner edge of a counterclockwise rotating torus feature. Masers at 6030 MHz are usually a factor of a few weaker than at 6035 MHz but trace the same material. Velocity gradients of nearby Zeeman components are much more closely correlated than in the ground state, likely due to the smaller spatial separation between Zeeman components. Hydroxyl maser peaks at very long baseline interferometric resolution appear to have structure both on scales smaller than that resolvable and on larger scales.

Subject headings: ISM: individual (W3(OH)) — line: profiles — magnetic fields — masers — radio lines: ISM — stars: formation

Online material: machine-readable table

1. INTRODUCTION

It is only in recent years that astronomers have recognized the importance of observing astronomical masers at very high spectral resolution. Such observations necessarily also require high angular resolution, as is achieved by very long baseline interferometry (VLBI), in order to minimize spatial blending of adjacent maser features, which may be separated by as little as a few milliarcseconds. Vlemmings & van Langevelde (2005) observed 22 GHz water masers at 0.03 km s^{-1} resolution with the Very Long Baseline Array (VLBA) in order to determine the line profiles, which give clues as to the saturation, beaming angle, geometry, and physical conditions at the maser site (Nedoluha & Watson 1991; Elitzur 1994; Watson et al. 2002; Watson & Wyld 2003). VLBA observations of 12 GHz methanol masers at 0.02 km s^{-1} resolution by Moscadelli et al. (2003) uncovered gradients in the positions of maser spots as a function of line-of-sight velocity, a phenomenon also observed in VLBI observations of formaldehyde masers (Hoffman et al. 2003).

W3(OH) is a good laboratory for studying maser phenomena. It contains a plethora of bright masers without substantial interstellar scatter broadening. It is also a close interstellar maser source whose distance has recently been measured to high accuracy by triangulation based on maser parallaxes: Xu et al. (2006) obtained a distance of 1.95 ± 0.04 kpc based on methanol maser parallaxes, while Hachisuka et al. (2006) derived a distance of 2.04 ± 0.07 kpc from water masers. (Henceforth, we assume a distance of 2.00 kpc for convenience.) For these reasons, W3(OH) has been a popular target for VLBI observations of OH masers in the ground state (Moran et al. 1968; Lo et al. 1975; Mader et al. 1978; Reid et al. 1980; Fouquet & Reid 1982; García-Barreto et al. 1988; Airapetyan et al. 1989; Bloemhof et al. 1992; Masheder et al. 1994; Wright et al. 2004a, 2004b; Fish et al. 2006a, hereafter FBS06), 4765 MHz (Baudry et al. 1988; Baudry & Diamond 1991; Palmer et al. 2003), 6030/6035 MHz (Moran et al. 1978; Desmurs et al. 1998, hereafter D98), and 13,441 MHz (Baudry & Diamond 1998) transitions, among numerous observations of OH masers at lower angular resolution.

Recently, FBS06 found key differences in the ground-state transitions of the interstellar OH masers in W3(OH) when observed at very high spectral resolution. Velocity gradients appear to be systematically smaller for 1667 MHz masers than for the other three transitions (i.e., 1667 MHz spots are more spread out in position over adjacent channels), matching predictions by Pavlakis & Kylafis (1996b). Another finding is that 1665 MHz masers typically have broader line widths than do the other ground-state transitions.

Contextualizing the empirical differences among the various transitions of OH may help constrain maser models and thereby provide additional insight as to the details of the physical processes involved in OH maser activity. This is our primary goal in obtaining similar observations of the 6030 and 6035 MHz masers in W3(OH) at very high spectral and spatial resolution. An additional goal is to obtain very sensitive VLBI observations of the 6.0 GHz lines to determine the distribution of maser features for comparison with previous and future epochs of data, both at 6.0 GHz and at other OH maser frequencies.

2. OBSERVATIONS

The EVN was used to observe the 6030.747 and 6035.092 MHz OH main-line masers in dual circular polarization in W3(OH). Eight stations were used: the Mk II telescope at Jodrell Bank, Effelsberg, the Onsala 25 m telescope, Medicina, Toruń, Noto, Darnhall, and a single Westerbork antenna. No usable data were obtained in left circular polarization (LCP) at 6030 MHz at the Mk II telescope due to a hardware failure.

The observing run (experiment code EF015) lasted for a total of 15 hours on 2006 June 11. W3(OH) was observed in a series

[1] Jansky Fellow.

TABLE 1
DETECTED 6030 AND 6035 MHz MASERS IN W3(OH)

Spot Number	Freq. (MHz)	Polar	R.A. Offset[a] (mas)	Decl. Offset[a] (mas)	Velocity[b] (km s^{-1})	Brightness[c] (Jy beam^{-1})	Vel. Gradient (km s^{-1} mas^{-1})	P.A.[d] (deg)	Zeeman Group[e]
1	6035	L	−973.59	50.73	−46.40	0.14	...	...	1
2	6035	R	−972.09	48.25	−46.13	0.19	...	...	1
3	6035	L	−961.91	40.38	−46.33	0.31	0.179	−73	2
4	6035	R	−961.57	40.33	−46.04	0.62	0.103	−73	2
5	6035	R	−955.93	91.60	−46.23	0.23	...	...	...
6	6035	R	−942.41	158.14	−46.50	0.30	...	...	3
7	6035	L	−942.23	159.55	−46.81	0.14	...	...	3
8	6035	R	−938.62	147.91	−46.04	0.22	...	...	...
9	6035	R	−934.46	169.20	−46.84	4.57	0.162	1	4
10	6035	L	−934.31	169.29	−47.15	2.29	0.149	5	4

NOTE.—Table 1 is published in its entirety in the electronic edition of the *Astrophysical Journal*. A portion is shown here for guidance regarding its form and content.

[a] Centroid of the Gaussian fit in the channel of peak emission. Right ascension and declination offsets are with respect to $02^h27^m03.8343^s$, $+61^\circ52'25.300'' \pm 0.01''$. Errors range from <0.01 mas for the strongest maser spots to $\lesssim 1$ mas for the weakest detections.

[b] LSR velocity of channel of peak emission.

[c] Peak brightness of the Gaussian fit in the channel of peak emission.

[d] Position angle is east of north in the direction of increasing line-of-sight velocity across the maser spot.

[e] See Table 2. Numbers in parentheses indicate unpaired masers in one transition, consistent with the central velocity and magnetic field strength derived from a Zeeman pair in the other transition.

[f] Reference feature.

[g] Consistent with $B = 8.3$ mG, $v_{\rm LSR} = -43.26$ km s^{-1} if interpreted as a multitransition Zeeman association.

of 25 minute blocks each followed by a 5 minute scan on the nearby calibrator J0207+6246. Seven 10 minute scans of the calibrator 3C 84 were interspersed for bandpass and single-band delay calibration. Sensitivity at the Noto telescope was sufficiently poor to prevent obtaining detectable fringes even on 3C 84, so no data from Noto were used.

Data were recorded with two-bit sampling of a 500 kHz bandwidth centered at $v_{\rm LSR} = -44$ km s^{-1} in both frequencies and both polarizations simultaneously. For maximum spectral resolution, the data were correlated in two separate passes, one for each frequency, at the Joint Institute for VLBI in Europe (JIVE). Each baseband channel was divided into 1024 spectral channels, for an equivalent channel separation of 0.024 km s^{-1}. A correlator averaging time of 2 s was used, which would be expected to produce negligible ($\sim$1%) brightness reduction due to time smearing at the location of the TW object, 7″ to the east (Turner & Welch 1984).

Data calibration was done in AIPS. The second calibration table (CL 2) from the EVN user pipeline, which contains a priori amplitude calibration (setting the absolute flux scale) and parallactic angle corrections but no fringe-fitting, was used as the starting point for subsequent data reduction. The calibrator 3C 84 was self-calibrated to produce a source model. Several minutes of data on 3C 84 were selected to compute the delay for each antenna using the source model in the task FRING. All data on 3C 84 were used (again with the source model) to determine a single complex bandpass correction for each antenna using BPASS. The bandpass correction was normalized to the inner 75% of the channels. Bandpass corrections were stable with time; a second scan-by-scan test run of BPASS on the bandpass-corrected data showed no apparent variations in the bandpass responses with time.

After running CVEL to apply the bandpass correction to the data and correct the velocities to the local standard of rest, a single channel in a single circular polarization containing bright maser emission in W3(OH) was SPLIT out. The data for this channel were self-calibrated. The resulting calibration was applied to all spectral channels in both circular polarizations of the same frequency, although 6030 and 6035 MHz data were calibrated independently. A large, lower spatial resolution and lower spectral resolution image was created using IMAGR with fields centered near W3(OH) itself and the TW object in order to identify regions of maser emission. Higher resolution images (2 mas pixels) in the subfields with detected maser emission were produced at full spectral resolution. The resulting natural-weighted synthesized beam width was approximately 7 mas. In each spectral channel, detected maser spots were fitted with elliptical Gaussians using a task based on JMFIT. In cases where the separation between two nearby maser spots is comparable to the synthesized beam width, elliptical Gaussians were fit simultaneously to both features.

The positional offset from the calibrator J0207+6246 was derived by fringe-fitting the bright reference maser spot used for self-calibration. The fringe-fit solution (phase and fringe rate) was applied to the calibrator. Time ranges of poor phase stability were flagged, and the remaining data were imaged. The apparent position of the calibrator was compared to the assumed position from the VLBA calibrator list,[2] derived from the Second VLBA Calibrator Survey (VCS2; Fomalont et al. 2003), to determine the absolute position of the reference maser feature.

Blank-sky noise ranges from 11 to 16 mJy beam^{-1}, depending on frequency, polarization, and spectral channel. These values are in line with theoretical noise levels from the EVN Calculator,[3] suggesting that the absolute flux scale is reasonable. However, dynamic range limitations dominate in many channels due to very bright emission, with noise levels exceeding 0.5 Jy beam^{-1} in some channels. Sidelobe contamination from the brightest spots is severe and may have contaminated the spectra of nearby maser spots centered near the same velocity.

3. RESULTS

The maser components we identify are listed in Table 1 and shown in Figure 1. The brightest masers, including the reference features at 6030 and 6035 MHz, are located in the cluster near the origin. No spots were seen near the TW object. Spectra of the maser emission, obtained by summing the flux density of all maser

[2] See http://www.vlba.nrao.edu/astro/calib/vlbaCalib.txt.

[3] See http://www.evlbi.org/cgi-bin/EVNcalc.

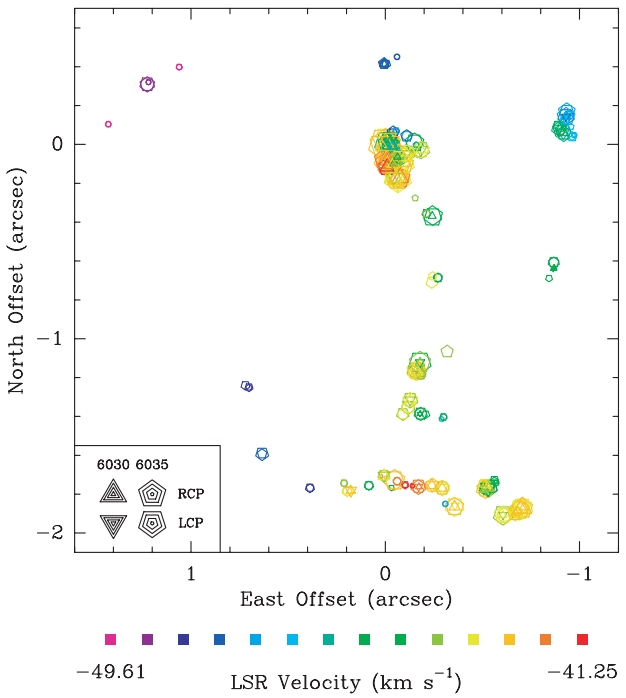

FIG. 1.—Map of detected 6030 and 6035 MHz maser emission in W3(OH). Symbol size is proportional to the logarithm of the peak brightness, with symbol sizes indicating 0.1, 1, 10, and 100 Jy beam^{-1}, shown in the lower left. LSR velocity is shown in color. LCP and RCP masers are each shown as open symbols for clarity. The center corresponds to R.A. = 02^{h}27^{m}03.8343^s, decl. = +61°52′25.300″ (J2000.0), with errors as detailed in § 3.1.

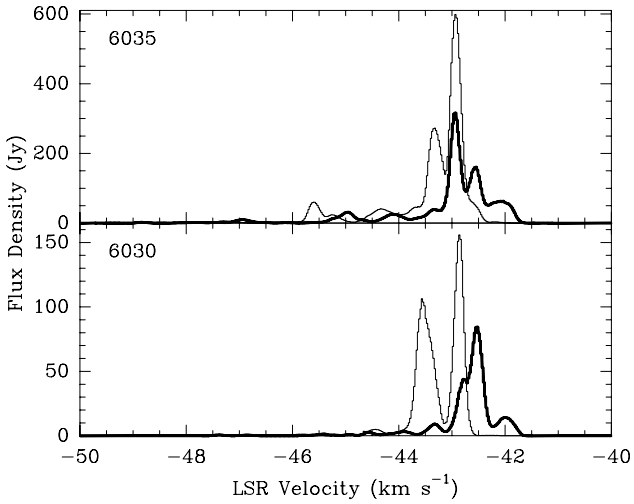

FIG. 2.—Spectra of maser emission in W3(OH) at 6035 (*top*) and 6030 MHz (*bottom*). RCP emission is shown in bold and LCP emission in normal weight.

spots detected, are shown in Figure 2. Overall, we find 90 spots at 6030 MHz and 202 spots at 6035 MHz associated with W3(OH). The weakest masers we detected have brightnesses of ∼100 mJy beam^{-1}.

3.1. *Comparison with Previous Studies*

There have been two previous VLBI studies of the 6.0 GHz masers in W3(OH). Moran et al. (1978) detected 12 Zeeman pairs at 6035 MHz with a three-element interferometer. D98 observed both main-line 6.0 GHz transitions with three elements of the EVN (Effelsberg, Mk II, and Medicina). Present observations exceed both previous observations in sensitivity and spectral resolution and produce a better sampling of the *uv*-plane.

The reference feature at 6030 MHz (spot 168, 82 Jy) is the brightest right-circular polarized (RCP) feature in that transition and was chosen in preference to the brighter left-circular polarized (LCP) feature in order that data from the Mk II telescope could be calibrated as well. The reference feature at 6035 MHz (spot 226, flux density 579 Jy LCP) is the brightest maser feature in W3(OH). We derive a position of R.A. = 02^{h}27^{m}03.8249^s, decl. = +61°52′25.217″ (J2000.0) for the reference spot at 6030 MHz and R.A. = 02^{h}27^{m}03.8343^s, decl. = +61°52′25.300″ (J2000.0) for the reference spot at 6035 MHz. Formal errors are approximately 1.5 mas, but this is likely an underestimate due to the poor quality of the images of the calibrator produced after fringe-fitting on the W3(OH) reference spots. We estimate that actual errors are approximately 10 mas, based on the offset needed to align overlapping Zeeman pairs at 6030 and 6035 MHz (Table 2), as discussed in § 3.3. The positions in Table 1 reflect this offset. Our positions agree with those of Etoka et al. (2005) to within 50 mas and with those of D98 to within 180 mas. For comparison, a typical maser motion of 3 km s^{-1} (Bloemhof et al. 1992) would produce a net motion of 4 mas between the epoch of observations of D98 and this work.

It is not possible to align the ground-state and excited-state data to milliarcsecond accuracy, since the ground-state data were not phase referenced in FBS06. Nevertheless, an approximate registration can be obtained from the similarity in distribution of the ground-state and 6.0 GHz data (Fig. 3). Masers at 6035 MHz are found both in regions where numerous ground-state masers occur and in regions where no ground-state emission is detected. However, 6035 MHz masers in different regions are seen in approximate superposition with each of the four ground-state transitions.

We can identify most of the features of D98 in our present data. Their reference feature at 6035 MHz (component A) corresponds to our spots 91 and 93, while their reference feature at 6030 MHz (component A′) corresponds to our spots 168 and 169. We note, as do Etoka et al. (2005), a systemic shift in local standard of rest (LSR) velocity of approximately 0.4 km s^{-1} in the D98 data. Figure 4 shows the motions derived from comparing our data with those of D98. Owing to differences in the positions of the reference features obtained in the two epochs, the absolute alignment of the maps of the two epochs of data is not known. Thus, the data are consistent with any set of motions differing from Figure 4 by the addition of a constant vector to all motions in each frequency (different at 6030 and 6035 MHz). We have chosen these constant vectors to minimize the rms motion, which is 10 km s^{-1}. The motions appear to be indicating fast counterclockwise rotation, in contrast with the 3–5 km s^{-1} expansion obtained from ground-state motions (Bloemhof et al. 1992). Wright et al. (2004a) noted a possible component of rotation based on 1665 MHz proper motions, although they interpret their motions as a *clockwise* rotation (i.e., north to south along the face of the continuum emission). In § 4 we argue that if the masers in the SE cluster in Figure 3 are part of this structure, rotation is in the counterclockwise sense. We do not discount the possibility that we have misidentified several maser spots between the two epochs partially due to spatial blending of maser spots in both epochs, although this would add random noise rather than a systematic bias to the derived motions.

3.2. *Variability*

Of the 292 detected features, 208 (71%) are brighter than 400 mJy beam^{-1}, the brightness of the weakest spot in D98, who

TABLE 2

ZEEMAN PAIRS AND ASSOCIATIONS

Group Number	R.A. Offset[a] (mas)	Decl. Offset[a] (mas)	Freq. (MHz)	Velocity[b] (km s^{-1})	B[c] (mG)	Separation (mas)
1	−972.84	49.49	6035	−46.27	4.7	2.9
2	−961.74	40.35	6035	−46.18	5.2	0.3
3	−942.32	158.84	6035	−46.66	5.6	1.4
4	−934.38	169.25	6035	−47.00	5.6	0.2
5	−930.58	143.36	6035	−47.18	6.0	0.2
	−930.44	142.61	6030	−47.11	6.2	0.1
6	−926.10	128.09	6035	−46.72	5.2	1.2
7	−918.27	59.06	6035	−45.44	6.5	0.1
	−916.70	60.34	6030	−45.65	6.1	0.1
8	−896.50	82.29	6030	−45.47	5.8	0.1
	−896.38	82.49	6035	−45.38	6.0	0.2
9	−867.20	−607.07	6035	−44.96	3.0	0.0
10	−865.84	−641.56	6030	−45.01	2.2	4.4
11	−705.08	−1871.16	6030	−43.08	6.1	0.3
	−705.04	−1872.15	6035	−43.11	5.6	1.2
12	−698.04	−1874.31	6030	−43.03	6.2	3.3
	−692.40	−1879.39	6035	−43.12	6.5	0.4
13	−679.09	−1892.51	6030	−42.97	6.4	1.5
14	−668.94	−1898.89	6035	−43.22	6.9	0.7
15	−612.22	−1907.35	6035	−43.47	6.0	0.7
16	−606.49	−1907.77	6030	−43.50	6.4	0.3
	−605.80	−1907.28	6035	−43.52	6.9	0.2
17	−568.86	−1742.78	6035	−44.81	4.7	1.1
18	−561.80	−1729.99	6035	−44.80	4.3	0.3
19	−534.33	−1765.18	6035	−44.42	3.9	2.3
20	−529.99	−1766.89	6035	−44.24	6.9	1.5
	−528.72	−1767.67	6030	−44.19	6.2	0.9
21	−515.88	−1772.23	6035	−42.64	6.9	0.3
22	−510.66	−1754.71	6035	−43.25	6.0	0.8
23	−506.15	−1779.58	6030	−44.07	4.9	0.5
24[d]	−357.89	−1861.65	6030	−43.04	2.2	7.3
	−356.97	−1864.87	6035	−43.18	6.0	0.2
25	−308.88	−1850.10	6035	−46.86	3.4	0.7
26	−299.61	−1402.92	6035	−45.47	4.7	0.7
27	−293.29	−1769.00	6030	−43.15	5.5	0.8
	−292.86	−1768.24	6035	−43.16	5.6	1.3
28	−271.07	−685.91	6035	−44.45	6.5	0.3
29	−243.72	−369.82	6035	−45.08	2.1	2.5
30	−240.79	−1754.80	6030	−42.71	6.1	0.6
31	−211.45	−355.09	6035	−44.06	6.5	0.5
32	−183.32	−1184.47	6035	−43.82	3.9	0.4
33	−183.33	−27.79	6035	−43.77	7.3	0.1
	−183.22	−28.10	6030	−43.73	8.0	0.0
34	−182.44	−1386.04	6035	−44.59	4.7	0.3
	−179.26	−1386.92	6030	−44.58	5.5	0.9
35	−181.92	−1175.25	6035	−43.81	5.2	1.9
36	−179.38	−1122.80	6030	−44.22	3.7	0.5
	−178.55	−1122.63	6035	−44.21	3.0	0.8
37	−173.06	−1762.18	6030	−42.11	4.3	1.2
	−170.82	−1761.36	6035	−42.04	5.2	0.1
38	−167.02	−1152.54	6035	−42.91	5.2	0.4
39	−160.86	−1166.89	6035	−43.07	5.6	0.8
40	−159.13	−2.55	6035	−45.96	6.9	0.4
41	−156.17	−1163.49	6030	−43.54	6.2	0.1
	−156.08	−1163.28	6035	−43.54	6.0	0.1
42	−155.36	−1176.45	6030	−43.04	5.2	0.9
43	−150.44	9.87	6035	−45.08	5.6	0.1
44	−139.63	−1757.14	6035	−41.40	5.2	1.2
45	−128.49	−1315.36	6030	−43.60	5.8	0.2
	−128.05	−1315.13	6035	−43.61	6.0	0.0
46	−117.50	−1352.74	6035	−43.56	6.0	0.2
47	−111.00	−45.81	6030	−43.53	8.3	0.2
	−110.62	−45.90	6035	−43.61	7.7	0.1
48	−101.93	−1752.86	6035	−41.43	4.3	0.4

TABLE 2—*Continued*

Group Number	R.A. Offset[a] (mas)	Decl. Offset[a] (mas)	Freq. (MHz)	Velocity[b] (km s^{-1})	B[c] (mG)	Separation (mas)
49	−95.01	−99.55	6035	−42.96	7.7	0.0
50	−90.56	−1387.55	6035	−43.64	6.0	0.1
51	−81.58	−62.85	6035	−43.56	8.6	0.2
52	−77.32	−171.96	6030	−42.51	6.5	0.2
	−73.66	−172.40	6035	−42.59	6.9	0.3
53	−69.40	−74.53	6035	−42.92	12.5	0.1
	−68.40	−75.01	6030	−43.04	13.2	1.0
54	−64.78	−80.71	6035	−44.33	8.2	0.8
55	−64.61	−175.44	6030	−43.04	8.3	0.3
	−64.38	−174.92	6035	−43.18	7.7	0.2
56	−62.94	−64.92	6035	−45.19	10.3	0.4
57	−60.84	−1733.41	6035	−42.17	4.7	1.0
58	−60.16	−34.87	6035	−46.78	10.7	0.2
59	−60.10	450.74	6035	−47.71	4.3	0.6
60	−58.08	−175.25	6035	−43.36	7.3	0.4
61[d]	−56.23	−81.94	6035	−44.67	12.5	0.5
	−54.23	−81.96	6030	−44.51	16.6	3.5
62	−47.48	−1727.98	6035	−42.64	5.2	0.6
63	−45.42	−103.48	6030	−44.40	10.1	1.1
64	−43.08	−169.52	6035	−43.56	7.7	0.4
	−42.63	−169.69	6030	−43.64	8.0	0.3
65	−39.74	61.55	6035	−48.01	7.3	3.9
66	−38.38	−103.75	6035	−43.89	6.5	2.7
	−37.68	−104.19	6030	−43.94	10.7	0.3
67	−36.37	−10.72	6030	−46.04	11.7	0.4
	−35.57	−9.85	6035	−45.94	11.2	0.4
68	−26.65	−0.54	6030	−44.98	10.8	0.0
	−26.39	−0.11	6035	−44.97	10.3	0.1
69	−23.57	13.70	6035	−45.72	9.5	0.3
70	−17.78	26.68	6035	−45.08	6.5	0.2
71	−9.98	5.89	6035	−45.41	6.9	0.2
72	−8.94	36.69	6035	−44.45	5.6	0.6
73	−8.87	−116.58	6030	−42.26	10.7	0.3
	−8.48	−115.99	6035	−42.13	11.2	0.3
74	−8.13	−96.63	6035	−42.25	11.2	0.1
	−7.81	−94.98	6030	−42.29	10.8	1.3
75	−7.14	−80.52	6035	−42.45	12.0	0.2
	−6.11	−78.59	6030	−42.46	10.7	0.8
76	−2.59	414.69	6035	−47.34	1.3	5.3
77	6.44	415.93	6035	−47.54	3.4	0.8
78	6.88	−1704.38	6035	−43.74	3.9	0.2
	6.64	−1704.89	6030	−43.68	4.3	0.2
79	8.82	414.67	6035	−47.59	6.0	2.5
80	84.58	−1755.70	6035	−44.47	4.7	0.7
81	176.75	−1781.94	6030	−42.82	4.0	0.2
82	195.69	−1783.96	6035	−43.46	4.7	0.1
83	212.19	−1743.59	6035	−43.78	3.4	1.0
84	387.73	−1767.97	6035	−48.04	−1.3	0.6
85	634.08	−1592.47	6035	−47.76	−0.9	0.1
86	1061.15	398.43	6035	−49.18	1.3	0.6
87	1219.29	320.59	6035	−48.66	−0.9	1.9
88	1225.55	309.64	6035	−48.82	−0.4	0.1
89	1426.06	104.19	6035	−49.57	−1.3	0.9

[a] Average of the right ascension and declination offsets of the LCP and RCP components of the Zeeman pair.
[b] Center LSR velocity of the Zeeman pair.
[c] Positive values indicate magnetic fields oriented in the hemisphere pointing away from the observer.
[d] See § 3.3 for a discussion of this Zeeman association.

identified 82 maser features with three EVN antennas. For comparison, 203 features (80%) brighter than 400 mJy beam^{-1} were seen in the four ground-state lines in FBS06. It is surprising that the number of 6.0 GHz masers above this flux threshold exceeds that of ground-state masers, and even more surprising that the brightest 6.0 GHz maser (over 575 Jy beam^{-1}) is far brighter than the brightest ground-state maser (<100 Jy beam^{-1}, from FBS06). Surveys of other regions at lower resolution indicate that 6035 MHz masers are on average much weaker and less common by a factor of 3 than 1665 MHz masers (Caswell 2001, 2003).

However, the two sets of observations are not cotemporal. Indeed, the 6.0 GHz masers in W3(OH) are becoming brighter

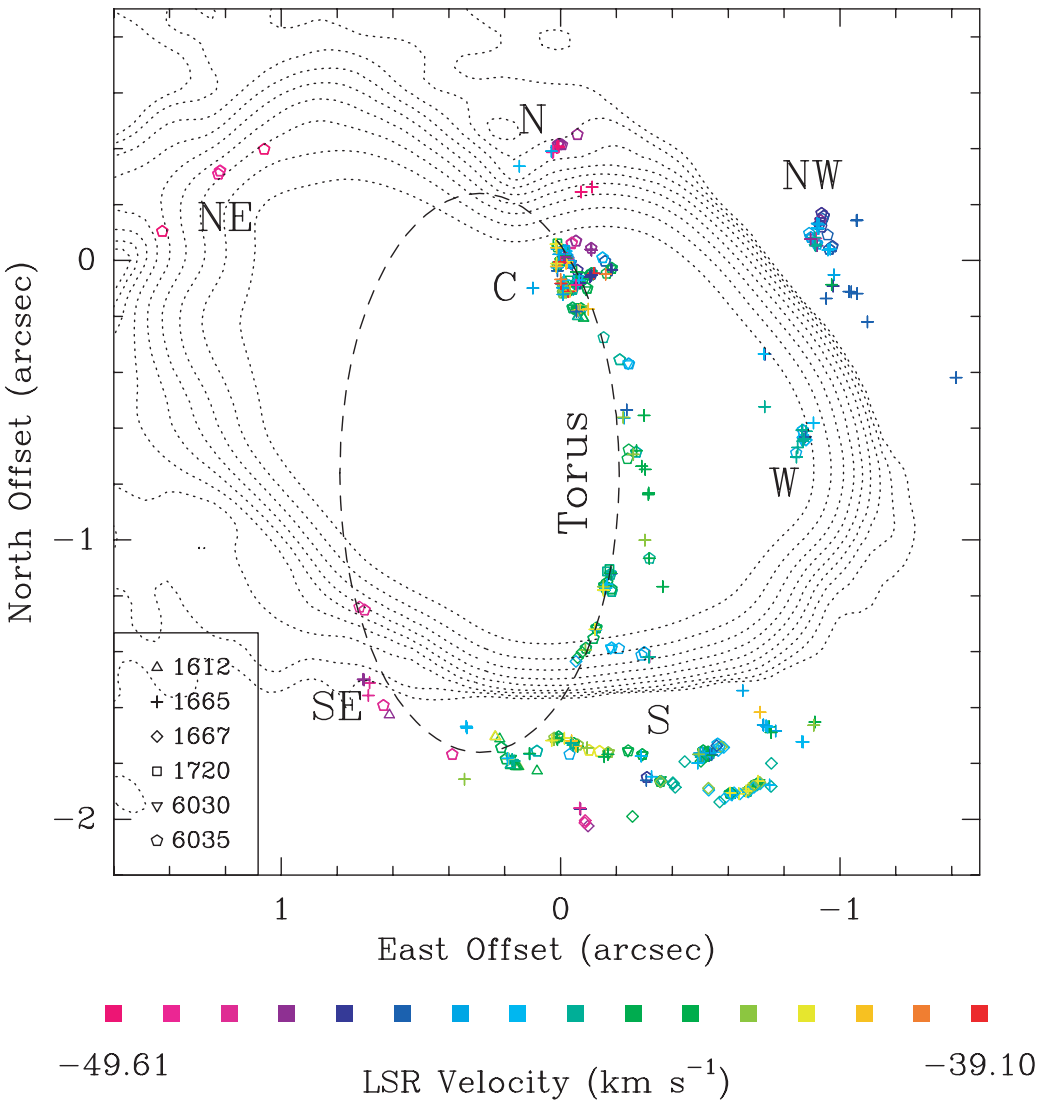

FIG. 3.—Map of 6030 and 6035 MHz masers, as well as ground-state masers (from FBS06), superposed atop 8.4 GHz continuum emission from the VLA archive (experiment code AR363; see Wilner et al. 1999). Velocities are not corrected for Zeeman splitting (see Fig. 16), which can be large (several kilometers per second) and unknown (due to unpaired Zeeman components) at 1665 and 1667 MHz. Dotted contours are shown at 4, 8, 16, . . . times the rms noise of 11.6 μJy beam^{-1}. Key maser groups and a potential torus feature (discussed in detail in § 4) as traced by the 6.0 GHz masers are indicated.

with time. Figure 5 shows the change in brightness for masers identified in both D98 and the current epoch (the same sample used to obtain proper motions). Many of the redetected masers are now approximately 4 times as bright as in the D98 epoch. As comparison of Figure 2 with the D98 Effelsberg autocorrelation spectra indicates, this is a real effect. Most masers that have become weaker are spatially blended with other maser spots in one or both epochs. This brightening is observed among 6.0 GHz masers in all regions of W3(OH), not just (for instance) the cluster near the origin (C). The D98 total power spectra also indicate a general brightening compared to the Moran et al. (1978) data, especially in the brightest LCP feature, although some individual features detected by Moran et al. (1978) are less bright in the D98 data.

3.3. *Zeeman Associations*

Zeeman pairs are listed in Table 2. Listed positions are the arithmetic mean of the locations of the LCP and RCP maser spots in each Zeeman pair. We identify a total of 117 Zeeman pairs, 35 in the 6030 MHz transition and 82 in the 6035 MHz transition. These include 28 Zeeman associations consisting of a Zeeman pair at each of 6030 and 6035 MHz. The difference in systemic velocity between the 6030 and 6035 MHz pairs is less than or equal to 0.10 km s^{-1} in 22 of the 28 full Zeeman quartets. The maximum velocity difference, 0.21 km s^{-1} in association 7, is still within a typical line width, and the slightly different positions and velocity gradients (in excellent agreement in magnitude and position angle between components of a Zeeman pair in one transition but not between components of different transitions) argue that the 6030 and 6035 MHz masers each trace different (although closely associated) material. Magnetic field values agree to within 1.0 mG or better in 24 of the 28 Zeeman associations. Including individual spots in one transition consistent with the magnetic field and central velocity at the same location in the other transition (given in parentheses in Table 2), 84% of maser spots are found in a Zeeman association.

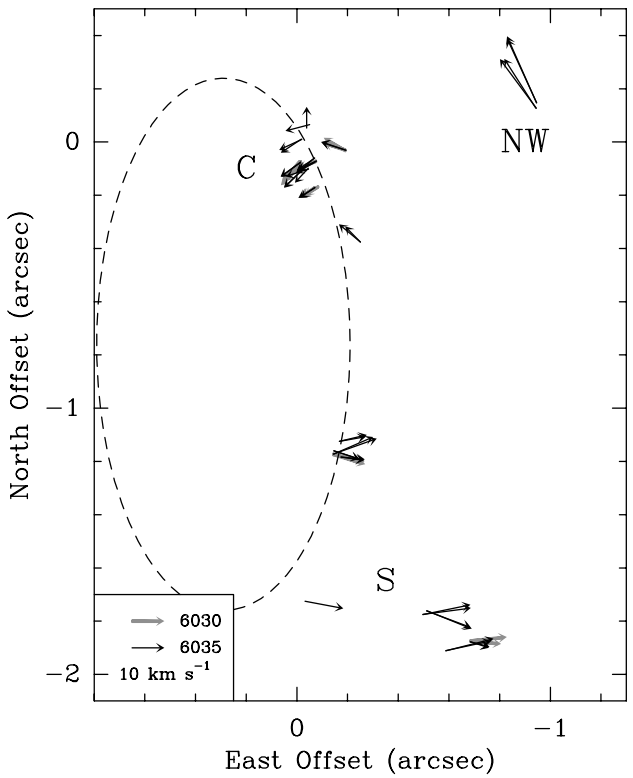

FIG. 4.—Motions of 6030 and 6035 MHz masers between the D98 epoch (1994 May 20–23) and the present observations. Vector length is proportional to velocity, with a 10 km s^{-1} motion indicated in the inset. The data are consistent with the addition of a single constant vector to the motions in each of the 6030 and 6035 MHz transitions. These constant vectors have been chosen to minimize the rms motions. The motions are not consistent with those obtained in the ground state by Bloemhof et al. (1992).

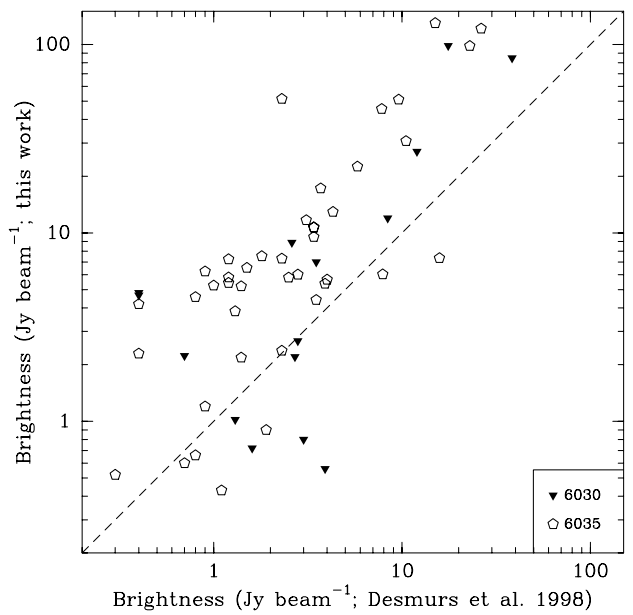

FIG. 5.—Variability of masers identified in both D98 and the present epoch. The dashed line indicates no change. Most masers have become brighter since the D98 epoch, assuming both flux scales are correct.

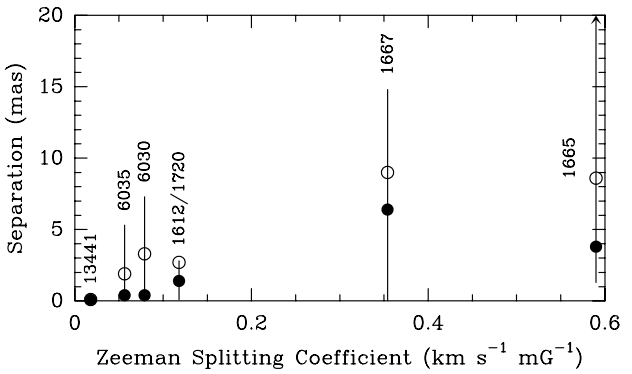

FIG. 6.—Separation between components of a Zeeman pair vs. Zeeman splitting coefficient. Lines indicate the range of separations, with median and 90% values indicated as filled and open circles, respectively. Satellite-line ground-state data are combined due to the small number of spots at 1612 and 1720 MHz. Zeeman pair separations increase with increasing Zeeman splitting coefficient. Ground-state data are from FBS06; 13,441 MHz data are from Baudry & Diamond (1998).

The median separation of components of a 6.0 GHz Zeeman pair is 0.4 mas (0.8 AU), with 90% of pairs having separations within 2.0 mas (4.0 AU). The 6.0 GHz Zeeman pairs have smaller separations than those in the ground state, as shown in Figure 6. The median separation between centers of 6030 and 6035 MHz Zeeman pairs in a Zeeman association is 0.9 mas (1.8 AU), with 90% within 3.0 mas (6.0 AU).

Masers at 6030 and 6035 MHz in Zeeman associations appear to be sampling the same material. In addition to being located at approximately the same location and sampling the same magnetic field, Zeeman pairs at 6035 MHz are brighter than, and preserve approximately the same brightness ratios as, their counterpart at 6030 MHz in Zeeman associations (Fig. 7). Comparison of the

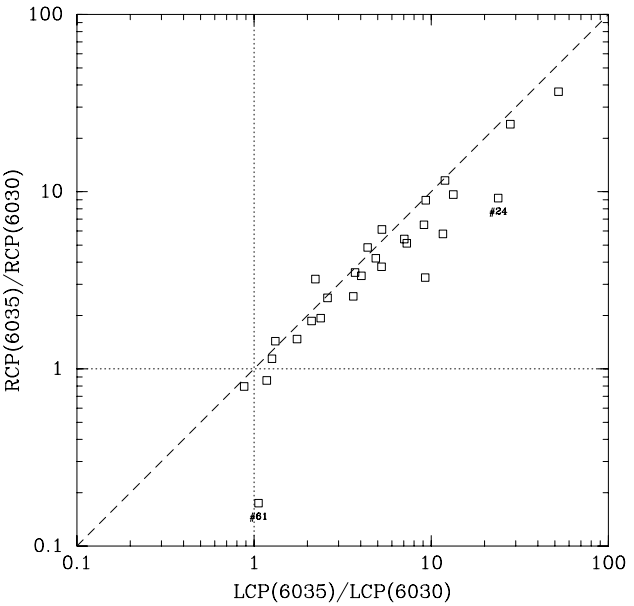

FIG. 7.—Plot of ratios of 6035 to 6030 MHz peak brightnesses of RCP vs. LCP spots in the 28 Zeeman associations consisting of a Zeeman pair at each frequency. Most points fall near the dashed line, which corresponds to equal amplification of the 6035 MHz Zeeman pair components compared to their 6030 MHz counterparts. The slight offset below this line is likely due to a small calibration error in the 6035 MHz RCP data. The dotted lines divide regions in which the 6030 and 6035 MHz masers dominate in brightness; in nearly every Zeeman association the 6035 MHz masers are brighter, usually by a factor of several. Zeeman associations 24 and 61, discussed in § 3.3, are labeled.

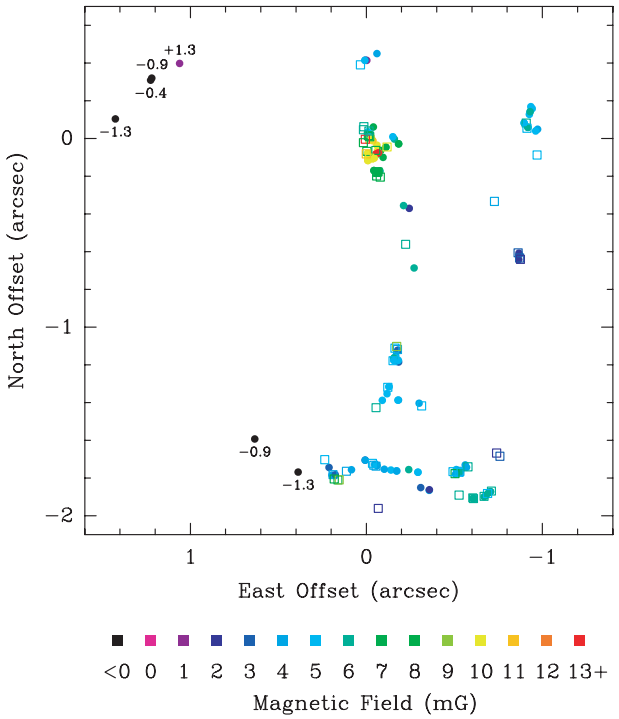

FIG. 8.—Magnetic field as determined from OH maser Zeeman splitting. Zeeman pairs at 6.0 GHz (this work) are shown as filled circles, and ground-state Zeeman pairs (FBS06) are shown as open squares. Colored symbols indicate the magnetic field strength (specifically, $\lfloor B \rfloor$ for positive magnetic fields) in increments of 1 mG. Negative values, indicating a line-of-sight magnetic field oriented toward the observer, are shown in black. Labels denote magnetic field values for Zeeman pairs 84–89.

VLBI maser spectra with Effelsberg autocorrelation data suggests that the slight offset from equal additional amplification in both polarizations at 6035 MHz compared to 6030 MHz is due to a larger fractional unrecovered flux at 6035 MHz RCP compared to the other polarization and transition. The largest outlier data point, Zeeman association 61 (Table 2), is located near the origin in Figure 8, where the magnetic field changes rapidly on a small spatial scale, differing by over 4 mG between the 6030 and 6035 MHz Zeeman pairs. It is probable that the 6030 and 6035 MHz pairs do not sample the same material in this association, given the discrepant magnetic field values obtained from their Zeeman splitting.

Zeeman association 24 also has a large difference between 6030 and 6035 MHz estimates of the magnetic field. We note that the spatial separation of the 6030 MHz Zeeman pair is the largest of any 6.0 GHz Zeeman pair (7.3 mas). The RCP component of this pair (spot 78) is significantly closer to the 6035 MHz emission and has an LSR velocity consistent with the central velocity and magnetic field derived at 6035 MHz. It is likely that spots 75 and 78 are not a true Zeeman pair but instead "Zeeman cousins" (opposite circular polarization components of two different Zeeman pairs in the same cluster of masers, as defined in Fish & Reid 2006).

Figure 8 shows a map of the magnetic field strengths as determined from 6030 and 6035 MHz Zeeman pairs. Magnetic field strengths are broadly consistent with previous observations, with the largest magnetic field strengths found near the origin. We do not find a systemic bias for higher magnetic field strengths in either transition compared to the other. Of the 28 overlapping associations of Zeeman pairs at both 6030 and 6035 MHz, 15 indicate larger magnetic field strengths at 6030 MHz and 13 at 6035 MHz. A similar conclusion was reached by D98.

Magnetic field values are nearly everywhere positive (i.e., in the hemisphere pointing away from the observer). However, we identify a total of five Zeeman pairs, all in the 6035 MHz transition, with the opposite line-of-sight field direction. The velocity range of the spots in these Zeeman pairs is very clean, so it is unlikely that sidelobe contamination has caused us to mistake their velocities. Spectra of these Zeeman pairs are shown in Figure 9. While several of the features in individual Zeeman pairs are weak, taken together the sample provides strong evidence for a line-of-sight magnetic field reversal in the source. Several of these pairs are located farther east than previous detections at lower (more negative) LSR velocity. Moran et al. (1978) claimed the detection of a Zeeman pair with a magnetic field of +2 mG in the northeast, but the separation between the two spots is 275 ± 100 mas, making it likely that the two spots are components of two different Zeeman pairs instead. Neither D98 nor Etoka et al. (2005) noted 6035 MHz masers at the velocities or locations of the negative magnetic field Zeeman pairs, although the Effelsberg autocorrelation data in Figure 1 of D98 show weak evidence of a feature near -49 km s^{-1} after correcting for the previously noted velocity shift. Three or four (depending on the exact velocity shift of the D98 data) of the five Zeeman pairs indicating a negative magnetic field in our data, including the only pair brighter than 1 Jy beam^{-1} in both circular polarizations, lie outside the velocity range imaged in D98. Fish et al. (2006b) also found evidence for negative magnetic fields at a velocity outside our observed range (-70 km s^{-1}) in the direction of W3(OH), although the association of these masers with W3(OH) itself rather than another source within the 130″ Effelsberg beam has not been confirmed interferometrically.

Comparison of the 6.0 GHz Zeeman data with ground-state data (FBS06) shows general agreement between magnetic field values. Where ground-state masers and excited-state masers overlap

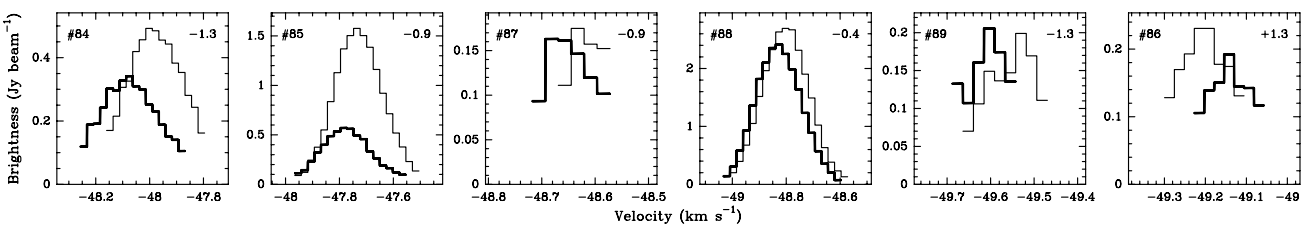

FIG. 9.—Spectra of Zeeman pairs indicating a negative magnetic field. RCP emission is shown in bold and LCP in normal weight. In the first five plots, the LCP emission is shifted to higher (less negative) velocity than the RCP emission, indicating a line-of-sight magnetic field oriented toward the observer. The Zeeman pair number (Table 2) and magnetic field (in milligauss) are indicated in the upper left and right of each plot, respectively. Zeeman pairs 84 and 85 are the easternmost Zeeman pairs in the southeast (SE) maser group of W3(OH). Pairs 87, 88, and 89 are the easternmost pairs in the northeast cluster (NE). The last plot, pair 86, indicates a positive magnetic field. This pair is the westernmost of the four Zeeman pairs in the northeastern cluster.

approximately, magnetic field strengths usually agree to within 1–2 mG, the principal exceptions being in the cluster near the origin in Figure 8, where the magnetic field varies greatly over small spatial scales. In the extreme southeast of the distribution of masers in W3(OH), Wright et al. (2004a, 2004b) found ground-state masers at velocities suggestive of a negative magnetic field. Our 6035 MHz data are consistent with this conclusion. As for the 13,441 MHz masers, we note that aligning the Zeeman pairs with a magnetic field of 7.7 mG in Baudry & Diamond (1998) near Zeeman pair 49 (7.7 mG) in Table 2 also produces excellent general agreement with the other Zeeman pairs in the Baudry & Diamond data. In particular, magnetic field strengths of 10.0 mG or greater in the Baudry & Diamond (1998) data match up near Zeeman associations 58, 67, and 68 in Table 2. Thus, while the 13,441 MHz OH masers preferentially trace material at higher magnetic field strengths than do the 6.0 GHz masers in W3(OH), the same set of physical conditions can be conducive to copropagation of 6030, 6035, and 13,441 MHz masers, a point supported by both theory and other observations (e.g., Gray 2001; Caswell 2004). A 10.3 mG Zeeman pair at 13,434 MHz centered at -42.21 km s^{-1} likely comes from the same area (Güsten et al. 1994; Fish et al. 2005).

A reanalysis of data from FBS06 shows no evidence of ground-state masers in the regions where 6035 MHz masers indicate a negative magnetic field. There are no ground-state masers in these regions brighter than 5 σ. Blank-sky rms noise levels are 20–30 mJy beam^{-1}, depending on transition, polarization, and spectral channel. Small velocity ranges containing very bright emission are dynamic-range limited and do not achieve theoretical blank-sky noise levels. Our usable bandwidth extends to $v_{\rm LSR} = -49.15$ km s^{-1} at 1720 MHz and -49.51 km s^{-1} at 1612 MHz, with 1665 and 1667 MHz edge velocities intermediate to these two values.

3.4. *Line Profiles*

For each maser line profile that is (near-)Gaussian in shape or has a clear (near-)Gaussian peak, we have fitted a Gaussian to obtain the FWHM (full width at half-maximum) of the peak of the profile. We obtain a FWHM line width for 169 of the 292 masers in our sample. Fits were done using brightnesses rather than flux densities, since nearly all masers are pointlike at our angular resolution (§ 3.5). Masers for which we do not obtain a measure of the FWHM have been excluded for one of several reasons. Some masers are too weak or have been detected in too few spectral channels to obtain good constraints on the fit parameters. Other masers have irregular or broad asymmetric spectral profiles or appear to consist of two or more Gaussian components of similar amplitude blended together. Some masers have profiles that are too heavily contaminated by emission from other nearby masers to obtain a good estimate of the line width.

The range of FWHM line widths of the 6030 and 6035 MHz masers in W3(OH) is 0.15–0.40 km s^{-1}, almost exactly the range of line widths seen in the ground state (FBS06). Bright masers do not in general appear broader than weak masers (Fig. 10), consistent with results of Baudry et al. (1997) and D98. The mean and sample standard deviations of the FWHM line widths are 0.235 ± 0.050 km s^{-1} at 6030 MHz and 0.229 ± 0.041 km s^{-1} at 6035 MHz. These values are in excellent agreement with those obtained at 1665 MHz (FBS06). For comparison, the 13,441 MHz masers have FWHM line widths of 0.24 ± 0.02 km s^{-1} (Baudry & Diamond 1998), consistent with the mean of 6.0 GHz masers but with less scatter. The distributions of line widths of 6030 and 6035 MHz masers are consistent with being identical with each other, a conclusion supported by Baudry et al. (1997) but not D98, who find broader 6035 MHz line widths. It is not clear where this discrepancy arises, although possibilities include the higher spectral resolution of our data as compared to that of D98, as well as our exclusion of distinctly non-Gaussian line shapes from our analysis. Our better uv-coverage and sensitivity may also provide less sidelobe contamination. In any case, blending of nearby maser components might be expected to broaden line widths more at 6035 MHz than at 6030 MHz due to the larger number of maser spots in the former transition.

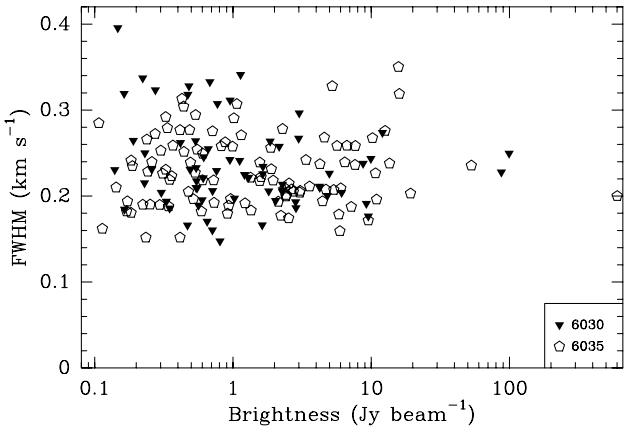

FIG. 10.—Distribution of FWHM maser line widths as a function of fitted brightness. As in the ground state (FBS06), there does not exist a strong correlation between line width and brightness.

Even maser spectra that look essentially Gaussian are normally not well fit with a single Gaussian profile. Figure 11 shows spectra of selected Zeeman associations. Line shapes range from near-Gaussian to asymmetric. In one case (Zeeman associations 39 and 41), double-peaked profiles at 6035 MHz are clearly indicative of spatial blending of two distinct maser spots. Other cases are less clear; see §§ 3.5 and 6 for a more complete discussion.

3.5. *Deconvolved Spot Sizes*

Most spots are unresolved with the EVN. Maser features with peak brightness greater than 1 Jy beam^{-1}, with a clearly detected peak in the spectral domain, and well fit spatially by a single elliptical Gaussian, are detected in a total of over 2000 spot channels. Of these, 83% have a nominal deconvolved spot size of zero, and 90% are consistent with a zero minimum deconvolved spot size. Thus, in the vast majority of cases, our spatial resolution is insufficient to determine the actual maser spot size.

When the minimum deconvolved spot size is greater than zero, it is still not clear whether we are detecting the finite size of a single maser spot or a blend of two unresolved, spatially separated spots. Figure 11 shows deconvolved spot sizes of masers in several Zeeman associations. In two of these cases (53 and 75), the 6035 MHz spots appear to have a finite size near line center. However, the line profiles are not well fit by a single Gaussian component. Our data cannot distinguish between a single spatially extended maser with a non-Gaussian spectral profile and a composite of several smaller masers with Gaussian spectra. In fact, it is not entirely clear whether these two cases are different, depending on what *a* maser is (§ 6).

3.6. *Saturation*

The saturation temperature of a maser is given by

$$T_s = \frac{h\nu}{2k}\frac{\Gamma}{A}\frac{4\pi}{\Omega},$$

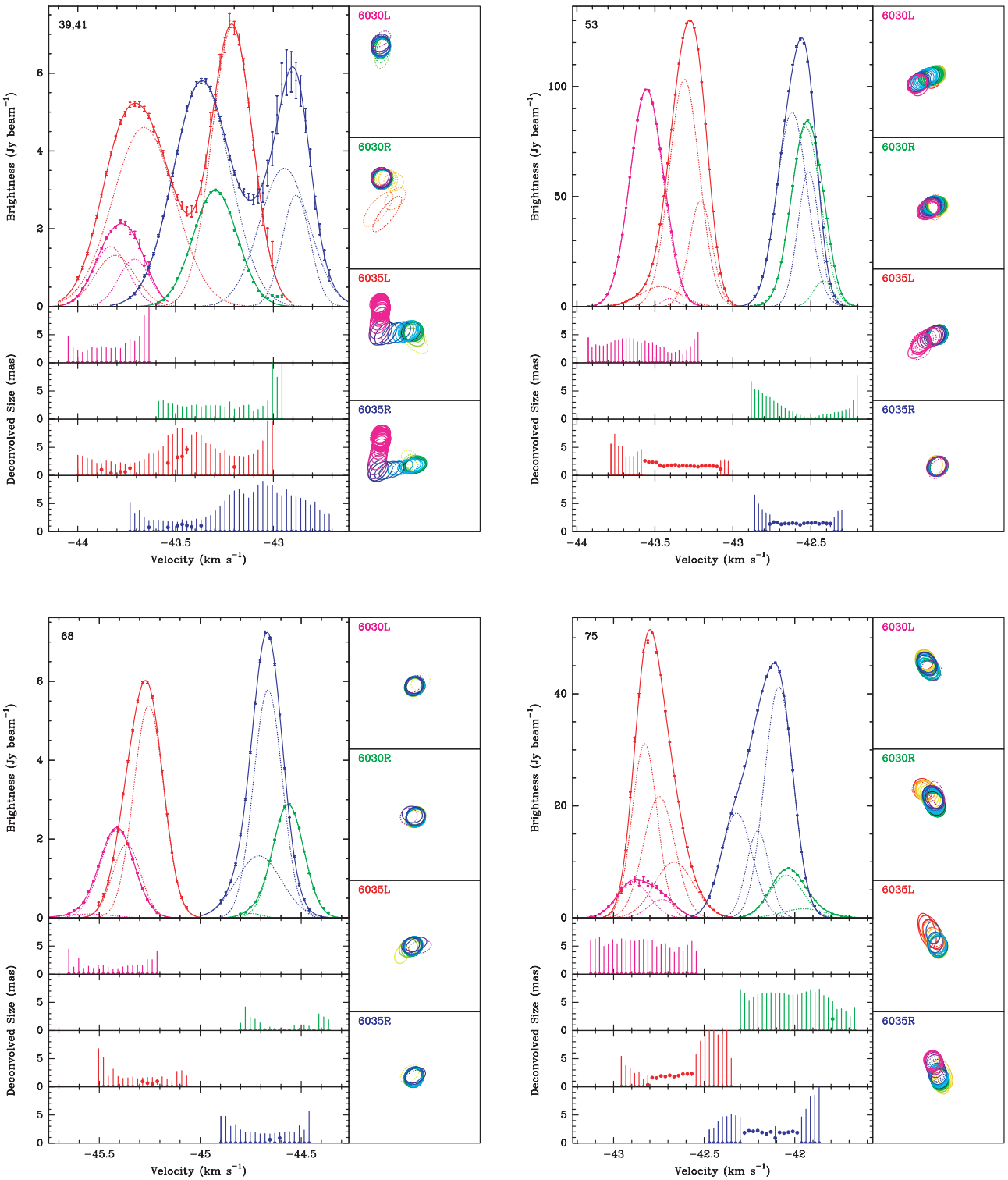

FIG. 11.— Composite plots of selected Zeeman associations. The upper left plots show the spectra of 6030 LCP (*magenta*), 6030 RCP (*green*), 6035 LCP (*red*), and 6035 RCP (*blue*) emission (*dots with error bars*), along with individual (*dotted lines*) and total (*solid lines*) Gaussian fits. The Zeeman association number is shown in the upper left. The bottom plots show the deconvolved spot size in each velocity channel for each transition /polarization (same colors). The nominal deconvolved spot size is shown as a dot, while the range of allowed deconvolved sizes is indicated by a vertical line. The plots on the right show the positions of the masers in each velocity channel. Boxes are 20 mas on a side, centered on the position of brightest emission in any transition and polarization. Relative positions are correct across transitions/polarizations. Ellipses are one-fifth the size of the undeconvolved fitted elliptical Gaussians. Color indicates velocity relative to the channel of peak emission (*shown in black*). Dotted ellipses represent channels with a S/N of less than 10 or in which emission is blended with a nearby feature (not shown).

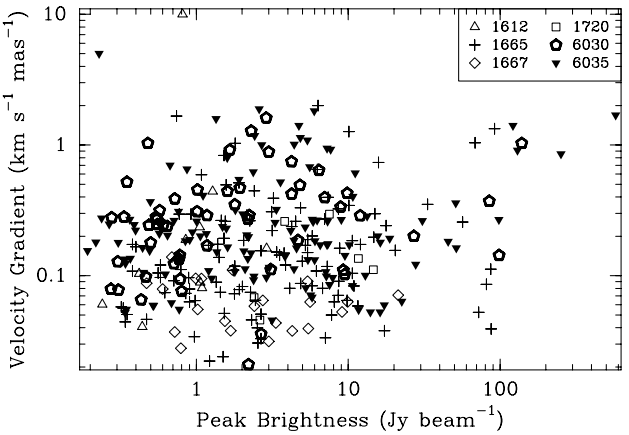

FIG. 12.—Magnitude of velocity gradient as a function of peak brightness. Thick symbols are from the present work; symbols in normal weight are from ground-state data from FBS06. There does not appear to be a correlation between the magnitude of the velocity gradient and the maser brightness. Velocity gradients at 1667 MHz are systematically smaller than in the other transitions.

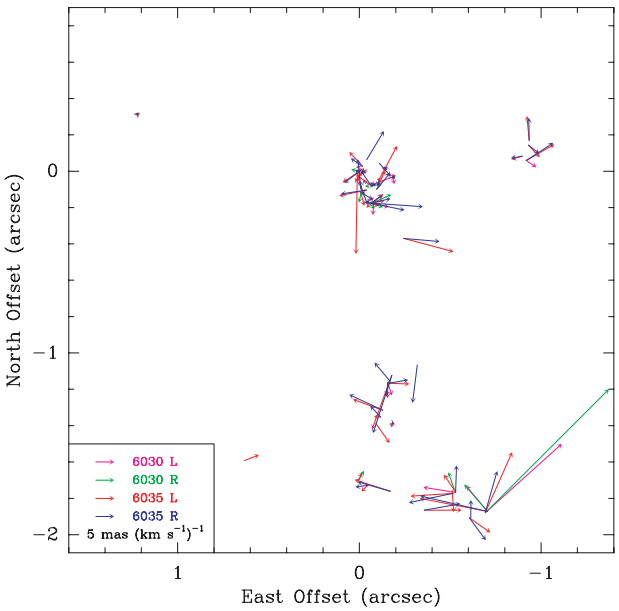

FIG. 13.—Map of positional gradients of spots with peak brightness greater than 1 Jy beam^{-1}. Arrows point in the direction of change with increasing line-of-sight velocity. Arrow length is proportional to the positional gradient, with sample vectors shown in the bottom left. Positional gradients are shown in lieu of velocity gradients (their inverse) to illustrate the excellent alignment of gradients of members of a Zeeman association (where arrow tails are nearly coincident). Positional gradients are typically smaller (velocity gradients are larger) in the cluster near the origin.

where Γ is the decay rate, A is the Einstein coefficient, and Ω is the beaming angle. Taking typical values of $\Gamma \approx 0.15$ s^{-1} and $\Omega \approx 10^{-2}$, the saturation temperature for a 6035 MHz maser is 1.7×10^{10} K (Reid & Moran 1988; D98). The brightest 6035 MHz maser we detect, with a flux density of 579 Jy in a maximum deconvolved size of 0.7 mas, corresponds to a brightness temperature of 5.7×10^{13} K and is clearly saturated. Its line width of 0.2 km s^{-1} indicates that saturated rebroadening to the thermal line width does not occur. Taking 2 mas as a reasonable upper size limit on a more typical 1 Jy maser results in a brightness temperature of 1.2×10^{10} K. This is comparable to the highest reasonable saturation temperature for a filamentary maser beamed toward the observer using a maximum amplification length of 10^{15} cm, the clustering scale of ground-state masers in W3(OH) as well as other interstellar OH maser sources (Reid et al. 1980; Fish & Reid 2006). D98 reached similar conclusions about the saturation of the 6.0 GHz masers in W3(OH) but note significant time variability in maser flux densities compared to observations taken 17 years prior. We note that long-term maser variability is common to a wide variety of maser species and transitions, including some very bright and clearly saturated masers (e.g., Garay et al. 1989; Alakoz et al. 2005; Fish 2007) and therefore does not constitute prima facie evidence against saturation. Another piece of evidence supporting saturation is provided by the preserved flux ratios between circularly polarized Zeeman components at 6030 and 6035 MHz (Fig. 7), which might not be expected if the masers were still operating in the unsaturated (i.e., exponentially amplifying) regime.

3.7. *Velocity Gradients*

Maser velocity gradients were measured following a method similar to that used by FBS06. In most cases, the gradients were determined algorithmically. We identified the nearest spectral channels on either side of the peak such that the brightness in those channels was less than half peak brightness. The velocity gradient was determined by dividing the LSR velocity difference of the two channels by the positional difference between them. Gradient magnitudes and position angles are reported in Table 1. Note that velocity gradients are inversely proportional to positional gradients, so a maser whose position changes rapidly as a function of LSR velocity will have a small velocity gradient (as measured in km s^{-1} mas^{-1}; 1 km s^{-1} mas^{-1} = 10^5 km s^{-1} pc^{-1}).

In some cases, spectral channels nearer to the peak channel were used to compute the gradient instead, for one or more of the following reasons: sidelobe contamination from a nearby strong maser feature, spatial blending with another maser feature, spectral blending with another feature at approximately the same location but at a different velocity, significant curvature of the locus of channel centroid positions, and poor determination of channel centroid positions in instances of low signal-to-noise ratio (S/N) detections. The use of spectral channels close to the peak channel in these instances preserves the intent of computing the local velocity gradient at line center. Velocity gradients were determined for a total of 178 masers out of the 292 detected, 37 of which required using a narrower range of spectral channels than the range of half peak brightness.

As with the ground-state transitions, there is no correlation between the brightness of a 6.0 GHz maser and its velocity gradient (Fig. 12). The range of magnitudes of velocity gradients in the 6030 and 6035 MHz transitions is comparable to that of the ground-state transitions. However, neither the 6030 nor the 6035 MHz masers display a propensity to occur only in regions of small velocity gradient (large positional gradient), as do 1667 MHz masers (FBS06).

Figure 13 shows the *positional* gradient of each maser spot for which it could be determined. The positional gradient is the natural observed quantity (the change in centroid position as a function of LSR velocity, measured in mas [km s^{-1}]$^{-1}$) and is the inverse of the velocity gradient (measured in km s^{-1} mas^{-1}). The error in determining the position angle of the gradient is small for a large change in the maser spot centroid as a function of LSR velocity (hence our decision to present positional gradients in preference to velocity gradients, where the largest gradients have large uncertainties in position angle). As seen in the ground state (FBS06), velocity gradients are typically larger (i.e., the positional

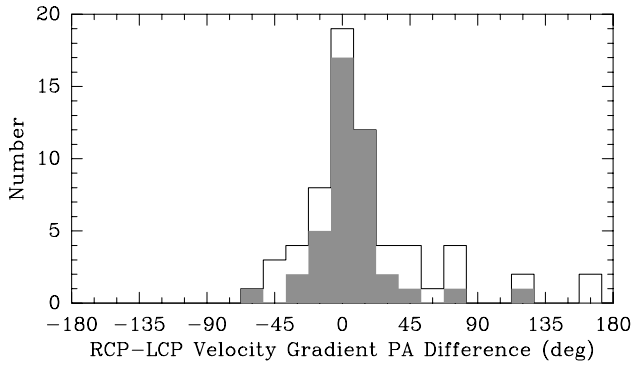

FIG. 14.—Histogram of position angle differences between the velocity gradients of the RCP and LCP components of a Zeeman pair. The distribution is strongly peaked near 0°, indicating that components of a Zeeman pair have correlated velocity gradients. The shaded area indicates the histogram for only those Zeeman pairs whose average velocity gradient is less than 0.3 km s^{-1} mas^{-1}. Since these spots have larger positional gradients, the error in determining position angles is smaller.

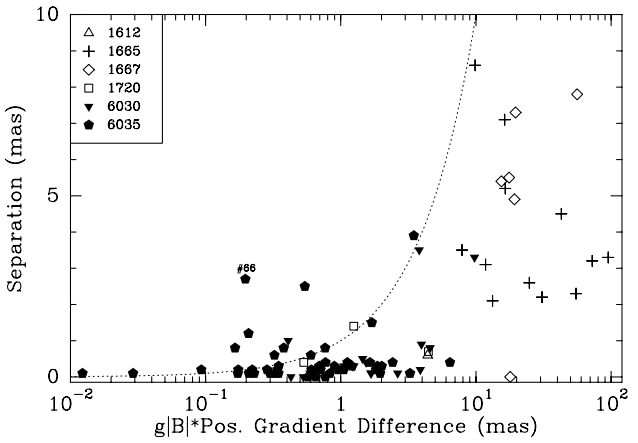

FIG. 15.—Separation of components of a Zeeman pair plotted against the expected spatial separation from the magnetic field. The abscissa is the velocity splitting due to the Zeeman effect multiplied by the vectorial difference of the positional gradients of the LCP and RCP components of a Zeeman pair. (Zeeman pairs with separations greater than 10 mas are not plotted, since these may be "Zeeman cousins" rather than true Zeeman pairs.) The dotted line indicates the locus of points for which the abscissa and ordinate are equal. Most spots fall under this line, indicating that $g|B|$ times the positional gradient difference is in most cases an upper limit to the expected spatial separation of Zeeman components. The largest outlier, labeled by Zeeman association number, is discussed in § 3.7.

gradient is smaller) in the cluster near the origin. Positional/velocity gradients are strongly correlated in a Zeeman association, both within a Zeeman pair (Fig. 14) and between Zeeman components in the two different transitions (6030 and 6035 MHz). This correlation can be seen visually in the example Zeeman associations in Figure 11. Velocity gradients show a stronger correlation between Zeeman components at 6.0 GHz than in the ground state (FBS06), likely due to the smaller spatial separation between Zeeman components. The correlation of velocity gradients is stronger still if only those pairs with small velocity gradients (i.e., large positional gradients) are considered, because small errors in determining the spot center in each channel are less important for these masers. However, velocity gradients do not show large-scale organization (unlike proper motions), suggesting that they trace local phenomena.

Figure 15 shows the transverse separation between components of a Zeeman pair as a function of the Zeeman splitting ($g|B|$, where g is the Zeeman splitting coefficient in km s^{-1} mG^{-1}, and B is the magnetic field strength in mG) multiplied by the magnitude of the vectorial difference in positional gradients in the plane of the sky (mas [km s^{-1}]$^{-1}$). This product represents the transverse splitting expected in the presence of a positional/velocity gradient due to Zeeman splitting. The LCP and RCP components of Zeeman pairs usually have a separation comparable to or smaller than this value. (The largest outlier in this plot is the 6035 MHz pair in Zeeman association 66, whose magnetic field as derived from Zeeman splitting is significantly different from that of the nearly coincident 6030 MHz pair, suggesting that physical conditions may change rapidly over a small spatial scale at this location.) Thus, the maximum separation between components of a Zeeman pair is roughly proportional to three quantities: the magnetic field strength, the Zeeman splitting coefficient, and the positional gradient (the inverse of the velocity gradient). This suggests an explanation for Figure 6: the separation between components of a Zeeman pair increases with the Zeeman splitting coefficient, but the 1667 MHz Zeeman pairs are even more widely separated due to the relatively large positional gradients (i.e., small velocity gradients, as in Fig. 12) seen in this transition.

3.8. *Linear Polarization*

Because our data were not correlated to produce cross-polarization (RL and LR) products, we cannot claim detections of linear polarization. However, we can comment on the lack of linear polarization from the signals in the RR and LL correlations alone. A maser spot with significant linear polarization (or unpolarized emission) would produce a detection in both LCP and RCP at the same LSR velocity. In the limit of a 100% linearly polarized spot, as would be expected for a pure π-component, the maser fluxes in both circular polarizations would be equal.

Of the 292 masers we detect, only six pairs of maser spots show this signature. Spots 253/256 constitute the clearest detection and may be due to a high linear polarization fraction in the 6035 MHz LCP reference feature. Much weaker linear polarization may be seen in the coincident 6030 MHz LCP feature (spots 251/254). In two other cases (spots 168/170 and 245/246) the peak brightness in the weaker polarization is less than 0.4% of that of the brighter polarization, which could be due to polarization leakage. Two weaker features at the same LSR velocity each have more equal LCP/RCP fluxes: spots 193/196 and 282/283. The former, located in cluster C with large magnetic field strengths, is likely due to linear polarization. The latter is located in cluster SE, which also hosts a 1612 MHz maser with large linear polarization (Wright et al. 2004b). However, we cannot rule out the alternative interpretation of Zeeman components separated by an undetectably small magnetic field, since the magnetic field strengths in cluster SE are smaller than throughout most of the source.

Thus, linear polarization appears to be rarer in the 6.0 GHz masers in W3(OH) than in the ground-state masers (García-Barreto et al. 1988; Wright et al. 2004a, 2004b). We do not note any 6.0 GHz linear polarization candidates in the NW cluster despite the fact that 1665 MHz masers in this cluster show linear polarization, although the 6.0 GHz masers are much weaker here than are the ground-state masers (García-Barreto et al. 1988). We also do not detect any π-component candidates. Wright et al. (2004a) found several spots at 1665 MHz with larger linear polarization than circular but also did not find any convincing π-component candidates.

4. STRUCTURE OF W3(OH)

Figure 16 shows the systemic velocities of Zeeman pairs in W3(OH). These velocities are uncontaminated with shifts due to

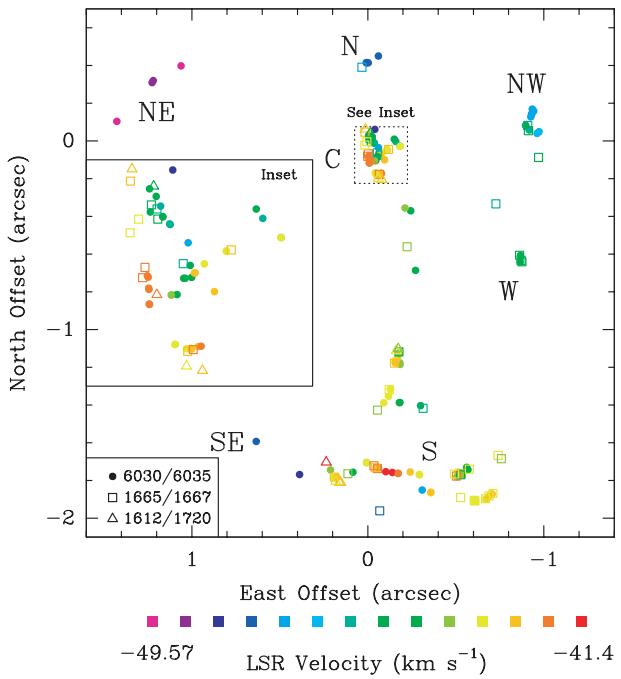

FIG. 16.—Systemic velocities of Zeeman pairs (i.e., average of LSR velocities of RCP and LCP components) in the six masing transitions at 1.6 and 6.0 GHz. Ground-state satellite-line masers (*triangles*) are seen only near the torus feature, while ground-state main-line masers (*squares*) are seen throughout W3(OH), excepting the NE cluster.

the Zeeman effect, which can be quite large (several kilometers per second) in the ground-state transitions. Several key features stand out. First, there is a large range of velocities in the central cluster, but there is also a clear gradient such that the velocity decreases toward the northwest. Second, velocities are clearly blueshifted in clusters NE, SE, N, and, to a lesser extent, NW. Third, many of the masers in S are redshifted, and maser velocities span a large range between S and SE.

Based on these features, the magnetic field (Fig. 8), and the distribution of 4765 MHz OH and 6668 MHz methanol emission (Harvey-Smith & Cohen 2005, 2006), we advance the following model for W3(OH). There is a ring-shaped structure, which we henceforth refer to as "the torus" (Fig. 3), that is well traced by the 6.0 GHz masers. The torus may be tracing a circular shock rather than, for instance, a density disk, but the masers nevertheless exhibit signs of counterclockwise rotation as viewed from the Earth. The structures labeled NW and S trace shocked molecular material in advance of the ionization front. The line of masers in S is seen to intersect the masers in the torus in projection and may be tracing a shock that intersects the torus in the third dimension and interacts with it. The masers in cluster N are found at the southern edge of a dense molecular condensation, while cluster C contains a similar, perhaps denser, condensation located just in front of the H II region. The masers toward the northeast are associated with the champagne flow. The remainder of this section is devoted to motivating this model.

The inner edge of the torus is delineated by the 6.0 GHz masers, where conditions (such as temperature or far-infrared flux) most favorable to excited-state emission are found. The apparent ellipse is roughly half as wide (east-west) as it is tall (north-south), indicating an inclination angle of $\sim 30^{\circ}$ to the line of sight, if circular, although the northern extent of the torus is uncertain. Much of the excited-state 4765 MHz emission is found in this region, including an extended filament oriented along the inner edge of the torus (Harvey-Smith & Cohen 2005). This contrasts with the 1665 MHz masers, which occur predominantly to the west of this edge, with the exception of the cluster near the origin. (In addition, some 6035 MHz masers are seen to the west of the inner edge of the torus, but these masers are weaker than those appearing on the edge itself.) All 26 satellite-line (1612 and 1720 MHz) masers in W3(OH) detected in FBS06 are found near this torus, despite the presence of other regions of strong main-line emission to the northwest and south. The satellite-line masers (Fig. 16, *triangles*) in the south have velocities consistent with being part of structure S rather than the torus itself, although the interaction between the two structures may be important. For completeness, we also note that Wright et al. (2004b) detected a weak 1720 MHz Zeeman pair in the cluster at the western edge of the bright continuum emission and a weak, highly redshifted (-41.48 km s^{-1}) 1612 MHz maser in the southern line of maser spots to the west of the torus.

The torus appears to be rotating in the counterclockwise sense. The masers projected along the face of the UCH II region have LSR velocities of ~ -44 km s^{-1}, slightly blueshifted from the presumed systemic velocity of -46 to -45 km s^{-1} (Welch & Marr 1987; Keto et al. 1995), a finding that is true for the 6668, 12,178, and 23,121 MHz methanol masers as well (Menten et al. 1988; Moscadelli et al. 1999; Harvey-Smith & Cohen 2006). The masers in cluster SE are very blueshifted, which would be consistent if their location is on the back side of the star-forming region, since counterclockwise rotation would give these masers a net velocity toward the observer compared to systemic. Cluster C is more complicated due to the gradient in LSR velocity to the northwest, a phenomenon noted also in methanol masers at 6668 and 12,178 MHz (Moscadelli et al. 1999; Harvey-Smith & Cohen 2006), which Moscadelli et al. (2002) modeled as conical expansion. It is not a priori clear whether the torus edge would be expected to pass through the center of this cluster or its inner (eastern) edge. We note, however, that all satellite-line (1612 and 1720 MHz) masers in cluster C appear along or near the inner edge, which is redshifted with respect to the systemic velocity of W3(OH) (see Fig. 16, *inset*). The sum of these properties is consistent with counterclockwise rotation, which is opposite to the direction of rotation assumed by Wright et al. (2004a) from 1665 MHz observations. However, their interpretation is based on 1665 MHz demagnetized velocities of ≈ -43 km s^{-1} to the south, which we argue are associated with feature S (not in the torus) rather than feature SE (part of the back side of the torus). Ultimate confirmation of the rotation will depend on a further epoch of proper motions, as Figure 4 does not provide information on the motions of the newly detected 6.0 GHz masers in the southeast of W3(OH).

Based on maser velocities, Wright et al. (2004b) speculated that the magnetic field is oriented toward the observer in the southeast, a finding we confirm from direct examination of 6.0 GHz Zeeman pairs. They also argue that these masers are located on the back side of the H II region, again based on their LSR velocities, which are blueshifted by several kilometers per second compared to the nearest masers as seen in projection (Fig. 3). While the H II region is probably optically thick at $\lambda = 5$ cm (e.g., Baudry et al. 1993), these masers are located south of or coincident with the H II region limb, so the ionized material is plausibly not sufficiently optically thick to prevent detection of masers from behind here, although the optical depth of the H II region may partially explain the weakness of these masers. The magnetic field polarity, negative behind the H II region and positive in front of it, indicates that the toroidal component of the magnetic field is oriented in the counterclockwise sense.

The torus model also can explain the filamentary 4765 MHz emission seen by Harvey-Smith & Cohen (2005). Diffuse, low-gain maser emission is seen along the torus, with peak emission near and north from declination offset $-1''$ at -44 to -43 km s^{-1}. (Emission is also seen on the eastern edges of clusters C and W.) The velocity is consistent with nearby OH and methanol masers, and the location is near where the rotating torus would be expected to have no net line-of-sight velocity with respect to the Earth. The presence of the diffuse maser emission may therefore be an indicator of a region of line-of-sight velocity coherence, a probable prerequisite for significant low-gain amplification.

We note that the torus does not necessarily trace a circumstellar disk. Linear or arclike structures with regular velocity structures suggestive of rotation have been noted in other maser sources, especially in methanol, and interpreted as circumstellar disks (Norris et al. 1993, 1998). However, mid-infrared imaging consistently indicates that these putative disk sources are associated with outflows and/or shocks instead (De Buizer 2003). It may be possible to obtain these maser structures if a shock oriented mostly perpendicular to the line of sight propagates through a rotating cloud (Dodson et al. 2004). The torus may therefore be tracing the interaction of an expanding shock with a rotating molecular structure, with a rapid falloff of density to the east. The distribution of ammonia absorption, seen over the western half of the H II region in W3(OH) but not the eastern half, supports this interpretation (Guilloteau et al. 1983; Reid et al. 1987). This pattern of absorption is seen in excited-state OH and formaldehyde as well (Guilloteau et al. 1985; Dickel & Goss 1987).

The inclination of the torus indicates that the western side of the torus is in front of the H II region or, equivalently, that the eastern side of the H II region is closer to the observer than the western side. The density of the surrounding material is lower to the east than to the west, as confirmed by several pieces of evidence. First, the density of ammonia seen in absorption falls off from west to east across the face of W3(OH), with particularly low values obtained toward the southeastern (SE) masers (Reid et al. 1987). Second, the ground-state masers in groups NW and S appear to be oriented along the limbs of the H II region where the radio continuum emission gradient is steepest, suggesting compression due to expansion into higher density material. Third, the expansion of the H II region is fastest toward the east (Kawamura & Masson 1998). Fourth, the champagne flow on the eastern side necessarily indicates a lower density to the east. This may also explain why the northeastern (NE) masers are especially blueshifted—they are located closest to the champagne flow (Wilner et al. 1999), where the ambient density is lowest, so they are accelerated most by the expansion of W3(OH). Indeed, an accelerated champagne flow model is supported by the recombination-line study of Sams et al. (1996). Fifth, the magnetic field along the putative maser torus is fairly consistently about 5 mG across the face of the H II region, except in cluster C, where it is larger. This would be expected if the density here is higher, which it almost certainly must be in order to support both very strong 6.0 GHz maser emission and 13.4 GHz masers (Baudry & Diamond 1998; Cragg et al. 2002; Wright et al. 2004a). But to the south along this arc, the magnetic field along the torus drops, below 5 mG for all six positive field values at 6.0 GHz (Zeeman associations 78 and 80–83). The two Zeeman pairs (numbers 84 and 85) indicating a negative magnetic field value both give magnetic field values of approximately -1 mG, indicating that the magnetic field (and therefore density) drop substantially to the southeast. Strong magnetic fields at 1612 MHz at the southern tip of the torus (Zeeman pairs 52–54 in FBS06) complicate the picture somewhat, but it is probable that these masers are actually associated with the structure labeled "S" in Figure 3, given that these masers are redshifted compared to the nearby masers in the torus and especially compared to the SE masers.

Cluster C is clearly a very energetic region. In addition to the OH masers at 1.6, 4.7, 6.0, and 13.4 GHz, there are weaker, extremely rare masers in the highly excited 7820 and 8189 MHz OH transitions (Baudry et al. 1993). This is, additionally, the region with the brightest methanol maser emission (Harvey-Smith & Cohen 2006). It is traditionally assumed that the main excitation source in the ionized region is near cluster C, based on the maser properties, higher magnetic field, and 23 GHz continuum peak (Guilloteau et al. 1983). It is perhaps not coincidental that the region of largest magnetic field strength occurs in cluster C, not far from the northern pinch.

Cluster N is likely at the periphery of a very dense region. It is probable that a region of high density is responsible for the prominent pinch in the H II region (see Fig. 3). The 6668 MHz methanol emission also provides indirect evidence of the high density. Bright 6668 MHz maser emission is cospatial with OH maser emission everywhere in W3(OH) *except* at cluster N (Harvey-Smith & Cohen 2006). The methanol maser emission nestles well into the pinch, and the OH masers (1665, 6030, and 6035 MHz) are found between the H II region and the dense clump. This scenario is supported by the model of Cragg et al. (2002), who found that warm material can support 6668 MHz methanol masers at densities higher by a factor of several than 1665 MHz masers, while other ground-state transitions, not seen in cluster N, require still smaller densities for maser activity. The 6.0 GHz masers in the region may sample slightly cooler, although still fairly dense, material located on the inside of the higher density methanol clump.

Besides the maser torus, large quantities of masers are seen in two regions: northwest (NW) and south (S) of the ionized region. In both of these regions, the limb of the ionized emission is very sharply defined (i.e., the contours of the radio continuum of the H II region are packed closely together in Fig. 3), and the distribution of maser spots is preferentially along, but offset about 400 AU from, the edge of the ionized region. This is consistent with expectations for the expansion of a *D*-type shock (Shu 1992). When the expansion speed of the H II region is less than twice the sound speed of the ionized region, both an ionization front and a shock front will be produced. The shocked neutral material between the fronts will often have conditions favorable to maser production (Elitzur & de Jong 1978). The typical expansion speed of both the ground-state masers (Bloemhof et al. 1992; Wright et al. 2004a) and the H II region itself (Kawamura & Masson 1998) is 3–5 km s^{-1}, substantially smaller than the sound speed in the ionized gas ($\sim$10 km s^{-1}; Yorke 1986). It is noteworthy that the southern line of masers and the northwestern clump are offset directly from the periphery of the H II region in areas where no expansion is seen in the Kawamura & Masson (1998) data (see their Fig. 3). The morphology and velocity structure of the masers in S are complicated and may be indicative of multiple shocks (or possibly a single shock with several regions of maser activity seen in projection) or energy input from an unseen source.

The masers indicating a negative magnetic field to the northeast are seen against continuum emission, albeit weaker emission than that seen over most of the face of W3(OH). It is not a priori clear whether these masers are located in front of or behind the continuum emission. While these masers are the most blueshifted of any 6.0 GHz masers seen in W3(OH), the lone Zeeman pair indicating a positive magnetic field in the region (Zeeman association 86; see Fig. 9) is intermediate in LSR velocity to the triad of Zeeman pairs indicating negative magnetic fields, suggesting that each of the four Zeeman pairs originates from the same side

(front or back) of the continuum emission as the others. It is possible that the magnetic field wraps around the front face of the ionized region here (as in Fig. 7 of Bourke et al. 2001), resulting in a reversal of the line-of-sight magnetic field direction. The density of the material in the NE cluster is clearly lower, as is supported by both the submilligauss magnetic field strengths and the existence of the champagne flow.

5. MULTITRANSITION MASER COMPARISON

Many theoretical models conclude that 6030 and 6035 MHz masers are excited under similar conditions (e.g., Gray et al. 1991; Pavlakis & Kylafis 2000; Cragg et al. 2002). Indeed, we find very close spatial association of 6030 and 6035 MHz masers, with typical separations being comparable to the separation within a single-frequency Zeeman pair and typical velocity differences much less than a line width after correcting for the Zeeman effect (§ 3.3). Masers at these two frequencies in Zeeman associations usually indicate similar magnetic field strengths and velocity gradients. The remarkable match in properties between 6030 and 6035 MHz masers admits the stronger conclusion that excitation of 6030 and 6035 MHz masers proceeds under similar conditions. It appears that, in fact, in many cases 6030 and 6035 MHz masers trace the same volume of gas, a conclusion that is not true for ground-state masers.

We do not find that 6.0 GHz masers prefer regions of either large or small velocity gradients, unlike 1667 MHz masers, which exist almost exclusively in regions of small velocity gradients (FBS06). This stands in contrast to the prediction of Pavlakis & Kylafis (2000) that inversion of both 6.0 GHz main lines requires a small velocity gradient. They model masers as cylinders of diameter 10^{15} cm with linear velocity gradients both along and across the cylinder [their $V = 1$ km s^{-1} corresponds to a velocity gradient of 3000 km s^{-1} pc^{-1}, or 0.03 km s^{-1} mas^{-1} at the distance of W3(OH)]. It is surely the case that the transverse size of the 6.0 GHz masers in W3(OH) is substantially smaller if they are cylindrical. The deconvolved spot sizes of our masers are consistent with being pointlike, indicating that actual maser sizes are at least a factor of several times smaller than the 7 mas (2×10^{14} cm) synthesized beam size. What is unclear, however, is whether velocity gradients in the plane of the sky correlate with velocity gradients along the line of sight. An observational bias may exist because a large velocity gradient along the line of sight would decrease the path length of velocity coherence for an OH maser, potentially rendering it undetectable; in principle, no such bias exists for velocity gradients transverse to the line of sight. On the other hand, this effect may be offset by velocity redistribution (Field et al. 1994; see also § 6).

Models also predict that 6030 MHz masers should be slightly weaker than 6035 MHz masers, a finding strongly confirmed in Zeeman associations in W3(OH) (Fig. 7), as well as surveys of other sources (e.g., Caswell 2003). Effectively, all 6030 MHz masers are accompanied with nearby, stronger 6035 MHz maser emission. The largest spatial separation between a 6030 MHz maser and the nearest 6035 MHz maser is less than 40 mas, but the 6030 MHz masers (Zeeman association 10 and spot 27) are especially weak. The 6030 MHz masers in Zeeman association 81 are also relatively weak (<1 Jy beam^{-1}) and separated from the nearest 6035 MHz by almost 20 mas. In all of these cases where 6030 MHz masers are found but 6035 MHz masers are absent, there is nearby 1665 MHz maser emission, matching a prediction by Pavlakis & Kylafis (2000). Three of these five 6030 MHz masers are not so weak as to prevent an estimate of the velocity gradient, which ranges from 0.027 to 0.054 km s^{-1} mas^{-1}. Caution is warranted in interpreting apparent velocity gradients of weak masers (the error in determining the position centroid in each channel is inversely proportional to the S/N), but the velocity gradients are nevertheless small, although at the low end of the range predicted by Pavlakis & Kylafis (2000).

Close spatial comparison with the ground-state masers is difficult because the absolute position of the data in FBS06 is not known, and the ground-state and 6.0 GHz maps cannot be aligned to milliarcsecond accuracy based on the location of Zeeman pairs. Nevertheless, the overall distribution of the masers matches closely enough (within a few tens of milliarcseconds) to permit some general statements to be made. The 1720 MHz masers in W3(OH) do appear to be located near (within 10–20 mas of) 6035 MHz masers, as predicted (e.g., Gray et al. 1991; Cragg et al. 2002). Zeeman pair 42 of FBS06 (6.6 mG) matches very well with Zeeman association 70 of the present work (6.5 mG), and spot 266 of the present work would indicate a 7.6 mG magnetic field if shifted from the systemic velocity of Zeeman pair 47 of FBS06 (6.8 mG). The other satellite-line masers at 1612 MHz also appear only in the general vicinity of 6035 MHz masers, although the spatial separation from the nearest 6035 MHz masers is at times larger than is true for the 1720 MHz masers. Masers in the 1667 MHz transition align with 6.0 GHz masers primarily in the southwest of W3(OH). Where 1667 MHz masers overlap with 6.0 GHz masers, they do so preferentially with associations in which both 6030 and 6035 MHz masers congregate. Nevertheless, the presence of both 6.0 GHz main-line transitions together does not predict 1667 MHz masers; for instance, numerous 6030/6035 MHz associations exist in the bright cluster near the origin and to a lesser extent in the center and northwest of W3(OH), but no 1667 MHz emission is found in these regions. In comparison, 1665 MHz masers are ubiquitous and appear in large quantities both in regions lacking 6.0 GHz emission and in regions where 6.0 GHz masers are plentiful, either as 6035 MHz masers alone or as 6030/6035 MHz associations.

All satellite-line masers detected by FBS06 are seen in the torus. This is likely due to the fact that the torus traces the inner edge of a region of high density. The differences between the locations of the 1612 and 1720 MHz masers may be related to the necessary pump processes. The 1720 MHz masers are found in two regions: cluster C and the edge of the torus near a declination offset of -1100 mas. Cragg et al. (2002) found that 1720 MHz emission requires a low kinetic temperature (or high dust temperature) and high OH specific column density, equal to the volume density of OH divided by the velocity gradient along the amplification length. This condition is likely achieved in cluster C due to a high molecular column density. Farther south, the high specific column density is likely partially due to velocity coherence along the line of sight, given the peak in 4765 MHz OH maser emission at this location (Harvey-Smith & Cohen 2005), as discussed in § 4. All 1720 MHz masers are found projected atop the H II emission, where far-infrared photons likely enhance the dust temperature. In contrast, Cragg et al. (2002) found that 1612 MHz masers also prefer regions of high specific column density but require a high gas temperature (or low dust temperature). Masers in the 1612 MHz transition are found in cluster C and where the torus intersects structure S. Again, the total column density in cluster C is very high, although it should be noted that the 1612 and 1720 MHz masers come from different parts of the cluster, satisfying the predicted conjugate behavior (Cragg et al. 2002). However, the 1612 MHz masers to the south are all located off the limb of the continuum emission and (with one possible exception in the southeast cluster) are probably associated with the interaction between the torus and structure S, which we argue is likely shock-driven and therefore consistent with a high gas temperature

and a low dust temperature. Thus, the locations of the 1612 and 1720 MHz masers support findings by Pavlakis & Kylafis (1996a, 1996b) that at high densities ($n_{H_2} > 10^6$ cm^{-3}) the 1612 MHz line can be excited by collisions alone, while inversion of the 1720 MHz line may be supplemented by infrared pumping.

6. MASER SUBSTRUCTURE AND SUPERSTRUCTURE

It is clear that the masers in W3(OH) have structure on scales smaller than those observed (e.g., § 3.5). Other maser transitions that have been observed in W3(OH), with higher angular resolution being achieved at higher frequencies, support this conclusion. Some 1665 MHz masers in W3(OH) are partially resolved at VLBI resolution, although others show deconvolved spot sizes of 3 mas or less (Reid et al. 1980; García-Barreto et al. 1988). The 1720 MHz masers show evidence for sizes less than 1.2 mas (Masheder et al. 1994). In other sources, the smallest intrinsic scales of structure are less than 2 AU [1 mas at the distance of W3(OH); Hansen et al. 1993; Slysh et al. 2001]. The highly excited 13,441 MHz masers in W3(OH) are as small as 400 μas (Baudry & Diamond 1998). Even some 12.2 GHz methanol masers in W3(OH) show evidence for submilliarcsecond structure (Moscadelli et al. 2002).

On the other hand, it is also clear that masers in W3(OH) have larger scale structure as well. Most of the 4765 MHz masers are larger than the synthesized VLBA beam (3–4 mas) and show flux on larger spatial scales than is observable with the VLBA (Palmer et al. 2003). The 13,441 MHz masers appear in filamentary or arclike structures up to several tens of milliarcseconds in size (Baudry & Diamond 1998). Extended structure is seen in 6.7 GHz methanol masers (Harvey-Smith & Cohen 2006), as well as in 12.2 GHz methanol masers (Moscadelli et al. 2002), with smaller ground-state and 6.0 GHz masers distributed along the filaments (Wright et al. 2004a, 2004b; Etoka et al. 2005; FBS06; this work).

Thus, the structures we see as masers likely both contain substructure and are themselves the bright, compact peaks of a larger structure. At our spatial and spectral resolution, the simplistic model of a maser profile as a narrow Gaussian begins to break down. Multiple components, possibly even a continuum of components whose parameters vary spatially, are required to model a maser line profile (see § 3.4 and Fig. 11, as well as Moscadelli et al. 2003). The question of what exactly constitutes *a* maser is not merely a philosophical one, but one that must be confronted in order to interpret modern observations. A detailed understanding of these effects is especially important for observers attempting to obtain geometric parallax distances from maser motions with respect to a distant background. Small changes in maser substructure may manifest themselves in apparent shifts of the maser centroid, limiting the accuracy to which such distances can be measured.

Maser observations with both very high spectral resolution and angular resolution provide a unique probe of conditions on AU scales. The velocity gradients that are seen may represent AU-scale turbulent fluctuations in the transverse velocity field. An analysis of the distribution and line-of-sight velocity scatter of water masers indicates that the inner scale of supersonic turbulent dissipation occurs at approximately 1 AU (Strelnitski et al. 2002), perhaps not coincidentally the size scale appropriate for OH masers as well. A similar analysis of maser transverse velocity gradients may permit estimation of parameters related to the inner turbulent scale. Understanding turbulence is important to understanding masers. Simple models of turbulence in a homogeneous medium can reproduce many observed maser properties (e.g., Böger et al. 2003), while a real star-forming region contains both turbulence and significant inhomogeneities in density, temperature, far-infrared photon flux, and other physical parameters. Future maser observations with very high spatial resolution, spectral resolution, and sensitivity may contribute greatly to our knowledge of maser processes.

7. CONCLUSIONS

1. The locations and velocities of the 6.0 GHz masers across the face and to the southeast of the continuum emission in W3(OH) support the model of a dense molecular torus put forth by Guilloteau et al. (1983) and Dickel & Goss (1987).

2. There is a reversal of the line-of-sight direction of the magnetic field in W3(OH), with positive magnetic fields (i.e., oriented away from the observer) in the west and negative magnetic fields in the east. The polarity of the magnetic field and demagnetized OH maser velocities at the inner edge of the torus suggest that the torus is undergoing net counterclockwise rotation.

3. Masers in the 6030 and 6035 MHz sample the same material. They are often found in direct spatial overlap and have nearly identical demagnetized LSR velocities, magnetic fields, and velocity gradients. Masers in the 6030 MHz transition are usually accompanied by stronger 6035 MHz emission, indicating that conditions conducive to masing in the 6030 MHz line are also conducive to masing at 6035 MHz, although with larger gain in the latter. Remarkably, even the ratio of circularly polarized components in a Zeeman pair in one transition is approximately preserved in the other.

4. The intrinsic sizes of 6.0 GHz masers in W3(OH) are considerably smaller than the synthesized beam size (7 mas = 14 AU). Line shapes are in many cases nearly Gaussian, with a line width of 0.15–0.40 km s^{-1}, although adequate line-shape fitting requires multiple (possibly a continuum of) Gaussian components. Most, if not all, detected 6.0 GHz masers are at least partially saturated.

5. Proper motions of 6.0 GHz masers are faster than motions at 1665 MHz (Bloemhof et al. 1992) and appear to be dominated more by rotation than expansion, a conclusion obtained at 1665 MHz by Wright et al. (2004a). A clearer picture of the kinematics of the 6.0 GHz masers will require another epoch of observations with the EVN. In particular, tracking motions of the south and southeast masers will greatly aid understanding of the nature and rotation (and possible expansion) of the torus, while tracking motions of the northeast masers will clarify their relation to the champagne flow.

6. W3(OH) hosts numerous OH masers with a range of densities, magnetic field strengths, pumping conditions, and gas motions all located within several hundred AU of the H II region, complicating simple interpretation in terms of the origin, structure, and evolution of W3(OH).

7. Masers are not just spots but trace a continuum of different structures of larger scale gas. Depending on physical conditions, they may appear most prominently as weak diffuse emission or strong compact objects. Future observations with high sensitivity, spectral resolution, and spatial resolution may allow estimation of turbulent parameters.

The European VLBI Network is a joint facility of European, Chinese, South African, and other radio astronomy institutes funded by their national research councils. The National Radio Astronomy Observatory is a facility of the National Science Foundation operated under cooperative agreement by Associated Universities, Inc. We thank W. F. Brisken for helpful comments in manuscript preparation.

REFERENCES

Airapetyan, É. A., Matveenko, L. I., Kostenko, V. I., Velikhov, V. E., Kopelyanskii, G. D., Molodyanu, A. P., & Timofeev, V. V. 1989, Soviet Astron. Lett., 15, 175
Alakoz, A. V., Slysh, V. I., Popov, M. V., & Val'tts, I. E. 2005, Astron. Lett., 31, 375
Baudry, A., Desmurs, J. F., Wilson, T. L., & Cohen, R. J. 1997, A&A, 325, 255
Baudry, A., & Diamond, P. J. 1991, A&A, 247, 551
———. 1998, A&A, 331, 697
Baudry, A., Diamond, P. J., Booth, R. S., Graham, D., & Walmsley, C. M. 1988, A&A, 201, 105
Baudry, A., Menten, K. M., Walmsley, C. M., & Wilson, T. L. 1993, A&A, 271, 552
Bloemhof, E. E., Reid, M. J., & Moran, J. M. 1992, ApJ, 397, 500
Böger, R., Kegel, W. H., & Hegmann, M. 2003, A&A, 406, 23
Bourke, T. L., Myers, P. C., Robinson, G., & Hyland, A. R. 2001, ApJ, 554, 916
Caswell, J. L. 2001, MNRAS, 326, 805
———. 2003, MNRAS, 341, 551
———. 2004, MNRAS, 352, 101
Cragg, D. M., Sobolev, A. M., & Godfrey, P. D. 2002, MNRAS, 331, 521
De Buizer, J. M. 2003, MNRAS, 341, 277
Desmurs, J. F., Baudry, A., Wilson, T. L., Cohen, R. J., & Tofani, G. 1998, A&A, 334, 1085 (D98)
Dickel, H. R., & Goss, W. M. 1987, A&A, 185, 271
Dodson, R., Ojha, R., & Ellingsen, S. P. 2004, MNRAS, 351, 779
Elitzur, M. 1994, ApJ, 422, 751
Elitzur, M., & de Jong, T. 1978, A&A, 67, 323
Etoka, S., Cohen, R. J., & Gray, M. D. 2005, MNRAS, 360, 1162
Field, D., Gray, M. D., & de St. Paer, P. 1994, A&A, 282, 213
Fish, V. L. 2007, in IAU Symp. 242, Astrophysical Masers and Their Environments, in press (arXiv: 0704.0242v1)
Fish, V. L., Brisken, W. F., & Sjouwerman, L. O. 2006a, ApJ, 647, 418 (FBS06)
Fish, V. L., & Reid, M. J. 2006, ApJS, 164, 99
Fish, V. L., Reid, M. J., & Menten, K. M. 2005, ApJ, 623, 269
Fish, V. L., Reid, M. J., Menten, K. M., & Pillai, T. 2006b, A&A, 458, 485
Fomalont, E. B., Petrov, L., MacMillan, D. S., Gordon, D., & Ma, C. 2003, AJ, 126, 2562
Fouquet, J. E., & Reid, M. J. 1982, AJ, 87, 691
Garay, G., Moran, J. M., & Haschick, A. D. 1989, ApJ, 338, 244
García-Barreto, J. A., Burke, B. F., Reid, M. J., Moran, J. M., Haschick, A. D., & Schilizzi, R. T. 1988, ApJ, 326, 954
Gray, M. D. 2001, MNRAS, 324, 57
Gray, M. D., Doel, R. C., & Field, D. 1991, MNRAS, 252, 30
Guilloteau, S., Baudry, A., & Walmsley, C. M. 1985, A&A, 153, 179
Guilloteau, S., Stier, M. T., & Downes, D. 1983, A&A, 126, 10
Güsten, R., Fiebig, D., & Uchida, K. I. 1994, A&A, 286, L51
Hachisuka, K., et al. 2006, ApJ, 645, 337
Hansen, J., Booth, R. S., Dennison, B., & Diamond, P. J. 1993, in Astrophysical Masers, ed. A. W. Clegg & G. E. Nedoluha (Berlin: Springer), 255
Harvey-Smith, L., & Cohen, R. J. 2005, MNRAS, 356, 637
———. 2006, MNRAS, 371, 1550
Hoffman, I. M., Goss, W. M., Palmer, P., & Richards, A. M. S. 2003, ApJ, 598, 1061
Kawamura, J. H., & Masson, C. R. 1998, ApJ, 509, 270
Keto, E. R., Welch, W. J., Reid, M. J., & Ho, P. T. P. 1995, ApJ, 444, 765
Lo, K. Y., Walker, R. C., Burke, B. F., Moran, J. M., Johnston, K. J., & Ewing, M. S. 1975, ApJ, 202, 650
Mader, G. L., Johnston, K. J., & Moran, J. M. 1978, ApJ, 224, 115
Masheder, M. R. W., Field, D., Gray, M. D., Migenes, V., Cohen, R. J., & Booth, R. S. 1994, A&A, 281, 871
Menten, K. M., Johnston, K. J., Wadiak, E. J., Walmsley, C. M., & Wilson, T. L. 1988, ApJ, 331, L41
Moran, J. M., Burke, B. F., Barrett, A. H., Rogers, A. E. E., Ball, J. A., Carter, J. C., & Cudaback, D. D. 1968, ApJ, 152, L97
Moran, J. M., Reid, M. J., Lada, C. J., Yen, J. L., Johnston, K. J., & Spencer, J. H. 1978, ApJ, 224, L67
Moscadelli, L., Menten, K. M., Walmsley, C. M., & Reid, M. J. 1999, ApJ, 519, 244
———. 2002, ApJ, 564, 813
———. 2003, ApJ, 583, 776
Nedoluha, G. E., & Watson, W. D. 1991, ApJ, 367, L63
Norris, R. P., Whiteoak, J. B., Caswell, J. L., Wieringa, M. H., & Gough, R. G. 1993, ApJ, 412, 222
Norris, R. P., et al. 1998, ApJ, 508, 275
Palmer, P., Goss, W. M., & Devine, K. E. 2003, ApJ, 599, 324
Pavlakis, K. G., & Kylafis, N. D. 1996a, ApJ, 467, 300
———. 1996b, ApJ, 467, 309
———. 2000, ApJ, 534, 770
Reid, M. J., Haschick, A. D., Burke, B. F., Moran, J. M., Johnston, K. J., & Swenson, G. W., Jr. 1980, ApJ, 239, 89
Reid, M. J., & Moran, J. M. 1988, in Galactic and Extragalactic Radio Astronomy, ed. G. L. Verschuur, K. I. Kellermann, & E. Bouton (Berlin: Springer), 255
Reid, M. J., Myers, P. C., & Bieging, J. H. 1987, ApJ, 312, 830
Sams, B. J., III, Moran, J. M., & Reid, M. J. 1996, ApJ, 459, 632
Shu, F. H. 1992, Gas Dynamics (Mill Valley: University Science Books)
Slysh, V. I., et al. 2001, MNRAS, 320, 217
Strelnitski, V., Alexander, J., Gezari, S., Holder, B. P., Moran, J. M., & Reid, M. J. 2002, ApJ, 581, 1180
Turner, J. L., & Welch, W. J. 1984, ApJ, 287, L81
Vlemmings, W. H. T., & van Langevelde, H. J. 2005, A&A, 434, 1021
Watson, W. D., Sarma, A. P., & Singleton, M. S. 2002, ApJ, 570, L37
Watson, W. D., & Wyld, H. W. 2003, ApJ, 598, 357
Welch, W. J., & Marr, J. 1987, ApJ, 317, L21
Wilner, D. J., Reid, M. J., & Menten, K. M. 1999, ApJ, 513, 775
Wright, M. M., Gray, M. D., & Diamond, P. J. 2004a, MNRAS, 350, 1253
———. 2004b, MNRAS, 350, 1272
Xu, Y., Reid, M. J., Zheng, X. W., & Menten, K. M. 2006, Science, 311, 54
Yorke, H. W. 1986, ARA&A, 24, 49